# Modeling and Characterization of Nonequilibrium Weld Microstructure Evolution

S. S. Babu[†], S. A. David[†], M. L. Santella[†], J. M. Vitek[†], E. D. Specht[†] and J. W. Elmer[††]

[†]Metals & Ceramics Division, Oak Ridge National Laboratory

Oak Ridge, TN 37831-6096

[††]Chemistry & Materials Science Department, Lawrence Livermore National Laboratory

Livermore, CA 94551-0808

*This paper is submitted for publication in the proceedings of 7th International conference on "Numerical Analysis of Weldability," Organized by IIW Sub commission IXB Working Group Chairman H. Cerjak, Co-Chairmen H.K.D.H. Bhadeshia, B. Buchmayr Graz-Seggau, 29th September to 4th October 2003*

# Table of Contents

## Abstract

The transition from equilibrium to nonequilibrium conditions often occurs during welding, depending on the cooling rate and weld metal composition. The present paper pertains to the in situ characterization of these transitions in complex alloys. With in situ measurements, it is possible to develop robust models that can describe microstructure evolutions for a generic weld metal composition and processing. Examples of weld microstructure evolution are presented for Fe-C-Al-Mn and 9Cr-1Mo-V steel welds. These microstructure evolutions were tracked by using time-resolved X-ray diffraction. Incomplete austenite formation was observed in the heat-affected zones of Fe-C-Al-Mn welds. Nonequilibrium austenite solidification was observed in the fusion zone of rapidly cooled Fe-C-Al-Mn welds. In slowly cooled welds, δ-ferrite solidification was observed. Presence of retained austenite was observed in 9Cr-1Mo-V in the weld metal region after normalizing treatment, which led to secondary martensite formation during tempering. In contrast, the austenite completely transformed in the 9Cr-1Mo-V base metal samples. Attempts were made to describe the above microstructure evolutions by using computational thermodynamics and kinetics models.

## Introduction

Weldability is defined as the capacity of material to be welded under the imposed fabrication conditions into a specific, suitably designed structure and to perform satisfactorily in the intended service [1]. Accordingly, numerical analysis of weldability must consider all of the above during welding [2, 3]. To meet this daunting goal, extensive work has been done in numerical analysis of arc-plasma-material interactions [4, 5, 6, 7, 8], heat transfer [9, 10, 11], mass transfer [12, 13], slag-metal equilibrium [14, 15], solidification [16, 17, 18, 19, 20], solid-state transformations [21, 22, 23], residual stress evolution [24], distortion [25, 26], and cracking and failure [27, 28, 29] in welded structures. The present paper deals with numerical analysis of weld microstructure evolution in steels. The weld microstructure evolution in both the fusion zone (FZ) and the heat-affected-zone (HAZ) of the welds have been modeled before by many researchers. These models relied on extending the equilibrium thermodynamic models so that inclusion formation and solidification segregation can be considered. Interface-response function models have been used to characterize phase selection and the extent of solute trapping during

solidification in rapidly cooled welds [30]. By coupling the thermodynamic models with the assumption of local equilibrium at the interfaces, the kinetics of microstructure evolution have been predicted during weld heating and cooling as well as during post-weld heat treatment (PWHT) [31. 32, 33]. Moreover, for low-alloy steels and stainless steels, the departures from local equilibrium to paraequilibrium have been considered in previous research to model austenite transformation to different ferrite morphologies [22, 34]. A review of past research shows that, in some cases, weld microstructure evolution may be closer to thermodynamic equilibrium and in some cases may depart from these conditions. Therefore, there is a need to develop reliable and experimentally validated models that can consider these conditions as a function of material composition, welding process, and process conditions.

In this paper, the experimental characterizations of weld microstructure evolution in two different steel systems and approaches to describe them using currently published thermodynamic and kinetic models are presented. First, the departure from the nonequilibrium solidification condition in Fe-C-Al-Mn steel weld will be presented. Secondly, the effect of microsegregation during solidification on nonequilibrium solid-state transformations during PWHT of 9Cr-1Mo-V steels will be presented.

The Fe-C-Al-Mn steel is relevant to the microstructure evolution in self-shielded flux-cored arc welds. Previous research in this steel system focused on inclusion and microstructural evolution [35, 36]. Microstructural characterization of welds with aluminum concentration less than 1 wt.% showed the presence of aluminum oxide and titanium carbonitride inclusions and classical $\alpha$-ferrite microstructure that forms from 100% austenite. In welds with an aluminum concentration greater than 1.5 wt %, aluminum nitride inclusions were present and the oxide inclusions were absent. In addition, the primary solidification through the $\delta$-ferrite phase was observed. With further cooling, incomplete transformation of $\delta$-ferrite to austenite takes place. As a result, the final microstructure of high-aluminum welds contained columnar $\delta$-ferrite. These microstructures were successfully predicted with computational thermodynamic and kinetic models [35]. The phase transformations that occur in the HAZ and the weld metal (WM) region of the high-aluminum gas-tungsten arc spot weld were evaluated with in situ time-resolved X-ray diffraction (TRXRD).

The 9Cr-1Mo-V (P91) steels are used in the super heaters of power boilers [37]. Because this steel is an air-hardenable martensitic high-strength alloy [38], the specifications of preheat and PWHT conditions are crucial [39,40]. One aspect of this issue is the handling of weldments between completion of welding and PWHT. Weldments that are cooled to room temperature before PWHT will transform more completely to martensite than weldments that are maintained at or above preheat temperature prior to PWHT. Consequently, weldments cooled to room temperature are less likely to contain untempered martensite after PWHT. However, maintaining preheat temperature before PWHT is essential for minimizing the probability of hydrogen cracking in weld HAZs. Adding to this complexity is the inherent difference between FZ and the original microstructure of the base metal (BM). The BM is in the wrought condition and in general does not contain remnants of as-cast solidification segregation. However, the FZ contains as-cast microstructure and may exhibit solute segregation. Both these microstructures may respond differently during PWHT. In this paper, the impact of FZ segregation on the transformation behavior during normalizing and tempering was studied by using a Gleeble® thermomechanical simulator equipped with a dilatometer and by using Synchrotron radiation to obtain in situ TRXRD measurements.

# Experimental

## *Investigation of Fe-C-Al-Mn Weld Microstructure Evolution*

The steel composition was Fe – 0.234C – 0.50 Mn – 1.70 Al – 0.28 Si – 0.02 Ni – 0.003 Ti – 0.006 O – 0.064 N (wt %). A surface layer was made on a 10.16-cm diam cylinder by depositing the above steel composition through the self-shielded flux-cored arc welding process. These cylinders were mounted on a fixture that was placed inside a chamber with a porthole allowing for X-ray entrance. Spot welds were produced on these bars to melt and resolidify the steel; the gas-tungsten arc-welding process was used. The average welding power was maintained constant at 1.9 kW (110 A, 17.5 V), and current pulsing was used to help minimize the side-to-side motion of the liquid weld pool. Helium was used as the welding and shielding gas, and a cross jet of helium was used to blow the evaporated metal powders away from the area where the TRXRD measurements were being made. In this experiment, the arc was extinguished 17 s after initiation. This step resulted in slow heating conditions in the HAZ and rapid cooling conditions

(> 1000 °C/s) in the FZ [41]. Additional experiments were performed to evaluate the effect of a reduced cooling rate in the FZ (< 100°C/s) by decreasing the welding current over a period of 25 s after the 17-s hold time. During these experiments, the phase transformation events were monitored by TRXRD). TRXRD measurements during welding were performed on a 31-pole wiggler 10-2 beam line [42] at Stanford Synchrotron Radiation Laboratory with the Stanford Positron Electron Accumulation Ring operating at an electron energy of 3.0 GeV and an injection current of ~ 100 mA. A 730-μm-diam pinhole was used, yielding a beam flux on the sample of $10^{10}$ to $10^{11}$ photons/s, as determined experimentally in an ion chamber downstream from the pinhole. A photon energy of 12.0 keV ($\lambda = 0.1033$ nm) was chosen to maximize the number of peaks diffracting into the 2θ window of the X-ray detector. Diffraction intensities at various 2θ positions were monitored continuously and in real time by a 5-cm-long photodiode array covering a 2θ range of approximately 30°. The diffraction spectra were collected at 0.05-s time intervals during transient heating and cooling of the spot welds. An overview of the experimental setup is shown in Fig. 1.

## *Investigation of 9Cr Alloy Weld Microstructure Stability*

The chemical compositions of the 9Cr alloys are given in Table 1. The submerged arc weld was made with Thermanit MTS3 welding filler metal (AWS A5.28, ER90S-B9) and Marathon 543 flux, both products of Böhler Thyssen. The 2-in.-thick plate used for the weldment was produced by Bethlehem Lukens Plate and is identified as BLP9Cr in Table 1.

**Table 1.** 9Cr Alloy chemical compositions

| | Analyzed composition, wt% | | | | | | | | | |
|---|---|---|---|---|---|---|---|---|---|---|
| ID/heat | C | Mn | Si | Cr | Mo | Ni | Nb | V | N | Al |
| Weld | 0.099 | 0.61 | 0.17 | 9.33 | 0.97 | 0.80 | 0.043 | 0.23 | 0.051 | 0.022 |
| BLP9Cr | 0.10 | 0.41 | 0.33 | 8.61 | 0.90 | 0.14 | 0.067 | 0.21 | 0.056 | 0.028 |
| 30383 | 0.083 | 0.46 | 0.41 | 8.46 | 1.02 | 0.09 | 0.072 | 0.198 | 0.051 | 0.002 |

The plates were prepared for welding with a single-V groove that had a 60° included angle. A total of 44 weld beads were used to complete the weldment. The weldment was given a PWHT of 8 h at 774°C (1425°F) before being supplied for the present investigation. Specimens from

normalized and tempered plate identified as heat 30383 were used to establish baseline transformation behavior for P91 plate.

A Gleeble® 3500 thermomechanical simulator was used to determine the temperatures where martensite starts to form during cooling (the $M_S$ temperatures). The Gleeble specimens used for this study were 6.35 mm (0.25 in.) diam × 108 mm (4.25 in) long rods. The rods were cut through the weld deposit transversely to the welding direction. Therefore, the heated portion of the specimen was within the weld deposit region. The dilation of the specimens during heating and cooling was measured with a linear variable dilation transducer (LVDT) strain gauge configured to detect changes in specimen diameter. A thermocouple was attached at the same location as the strain gauge along the specimen length. The specimens were heated either in a vacuum or in an argon atmosphere to minimize oxidation during testing. Transformation temperatures were determined by curve-fitting procedures at points of significant discontinuity on dilation vs temperature data plots.

The 9Cr alloy samples were subjected to similar heat treatments (i.e., similar to those used for dilatometry) while the in situ TRXRD was being performed in the synchrotron beam line. The resistive heating method was used to heat the samples in a preprogrammed cycle. A schematic illustration of the experimental setup is shown in Fig. 2. The sample was held in a flowing He atmosphere to minimize oxidation. X rays with wavelength $\lambda = 0.041328$ nm were provided by the UNICAT X-33 undulator beam line at the Advanced Photon Source. At that energy, X rays penetrate 0.16 mm into steel, so diffraction from the near-surface region is relatively weak. X rays were incident at a 7.5° glancing angle. A 2D image of the diffracted X rays was recorded every 8 s. Diffracted X rays were filtered with aluminum foil to remove fluorescence and were recorded by a Princeton Instruments model SCX-1242E CCD camera with 1152 × 1242 pixels, a 0.0225 × 0.0225 mm pixel size, and 16-bit resolution. The detector was placed 97 mm from the sample; measuring plane spacing was in the range of $0.10 \text{ nm} < d < 0.25$ nm. Silicon powder was used to calibrate the detector (NIST SRM 640b, $d = 0.54311946$ nm). The 2-D diffraction rings were summed to obtain $2\theta$ intensity plots. During measurement, weak diffraction appears from $(Fe, Cr)_2O_3$, which is formed from residual $O_2$ in the He atmosphere.

# Modeling of Weld Microstructure Evolution

## *Austenite Formation in the HAZ of Fe-C-Al-Mn Welds*

The equilibrium thermodynamic phase evolution was predicted by using ThermoCalc® software [43] version P with the solid solution database [44]. The calculations considered equilibrium between liquid, ferrite (bcc), austenite (fcc), and cementite ($Fe_3C$). In addition to equilibrium thermodynamic calculations, the diffusion controlled growth of ferrite to austenite during the weld heating was simulated by using DicTra® software [45]. In these calculations, solid solution thermodynamic databases and standard mobility databases were used. The geometry used for the simulation is shown in Fig. 3. In this case, the room-temperature microstructure is taken as a mixture of ferrite and 14% martensite based on optical microscopy analysis. The carbon concentration of ferrite was fixed at 0.03 wt %, based on thermodynamic calculations at 800 K. The carbon concentration of martensite was fixed based on nominal composition and ferrite fraction. The simulations were performed with two assumed thermal cycles. The first thermal cycle considered single-stage heating until a peak temperature of 1740 K. The second thermal cycle considered two-stage heating, which consisted of a rapid heating until 1510 K and then slow heating to 1520 K. The two-stage thermal cycles are similar to the results presented by Zhang et al. [41] for C-Mn steel spot welds and recent finite different simulation of a spot weld [46]. It is important to note that these heating rates are approximate.

## *Phase Selection in Fe-C-Al-Mn welds.*

Since the current research in Fe-C-Al-Mn steel pertains to the weld solidification, it is necessary to consider different phenomena that can occur under different cooling rates to describe the transition from equilibrium to nonequilibrium conditions. Most relevant nonequilibrium solidification features in welding that occur due to increased liquid-solid interface velocities under rapid cooling conditions [47] are as follows.

- Elemental partitioning ($k$ = solid composition/liquid composition) for a given velocity ($k_V$) increases from the equilibrium value ($k_{eq}$) and reaches unity at high velocities; $k_{eq} < k_V < 1$ [48, 49].
- Primary solidification of a nonequilibrium phase may occur [50].

- Liquid-solid interface morphology changes from planar to cellular to dendrite and back to planar with increasing solidification velocity [51].
- In some steel welds, mixed bands of ferrite and austenite may also occur [52].

In reality, all these phenomena are interrelated and influence each other during weld solidification. To describe these changes, we have adopted a previously published interface-response function model [30] that predicts the solid-liquid interface temperature as a function of velocity. In this model, a set of equations describing different phenomena is considered and solved for unique dendrite tip temperature, radius, and velocity data pairs. The procedure is briefly given below. For details, the reader is referred to references 53, 54, 55, and 56.

The velocity-dependent partitioning coefficient ($k_V^i$) is related to $k_o^i$, the equilibrium partition coefficient for each alloying element "*i*" in the liquid/solid boundary; $a_o$ is the characteristic diffusion distance, $D_i$ is the solute diffusivity at the liquid/solid boundary for element "*i*", and $V_s$ is the solid-liquid interface velocity as given below.

$$k_V^i = k_o^i + a_o\left(V_s/D_i\right)\Big/\left[1 + a_o\left(V_s/D_i\right)\right] \tag{1}$$

The velocity-dependent liquidus slope for a given $i^{th}$ element is related to equilibrium liquidus slope ($m_V^i$), velocity-dependent partitioning coefficient, and equilibrium partition coefficient as follows.

$$m_V^i = m_o^i\left(1 - k_V^i\left(1 - \ln\left\{k_V^i/k_o^i\right\}\right)\right)\Big/\left(1 - k_o^i\right) \tag{2}$$

The velocity-dependent dendrite tip radius is related to the Gibbs-Thompson coefficient ($\Gamma$). $Pe^i$ is the Peclet number for each alloying element given by the relation $Pe^i = V_s R/2D_i$ as given by Eq. (3). In the present work, the boundary diffusivity ($D_i$) was assumed identical for all the alloying elements. The parameter $\xi_C^i$ is a function of the solute Peclet number as given in [57]. The parameter *G* in Eq. (3) is the temperature gradient.

$$4\pi^2\Gamma\left(1/R^2\right) + \left(2\sum_i\left[m_V^i Pe^i\left(1 - k_V^i\right)c_l^{i*}\xi_C^i\right]\right)\left(1/R\right) + G = 0 \tag{3}$$

The velocity-dependent ($c_l^{i*}$) liquid/solid interface concentration for $i^{th}$ alloying elements is related to $Iv\{Pe^i\}$, which is the Ivantsov function that depends on the Peclet number and velocity-dependent partitioning coefficient:

$$c_l^{i*} = c_o^i \Big/ \left[1 - \left(1 - k_V^i\right) Iv\{Pe^i\}\right] \tag{4}$$

Finally, the velocity-dependent dendrite tip temperature is related to all the above parameters as well as the equilibrium liquidus temperature ($T_l$) of the initial alloy composition, the interface kinetic coefficient ($\mu$), and Gibbs-Thompson coefficient ($\Gamma$) as given below.

$$T_{d/c} = T_l + \sum_i \left(c_l^{i*} m_V^i - c_o^i m_o^i\right) - 2\Gamma/R - V_s/\mu - GD/V_s \tag{5}$$

In the present work, ThermoCalc® software version P [43] was used to calculate the equilibrium liquidus temperature ($T_l$), slope ($m_o^i$), and partition coefficient ($k_o^i$) at $T_l$ as a function of the steel composition. Equations (1) through (5) were solved iteratively by using numerical techniques. If the ferrite dendrite-tip temperature (either $T_{d/c}$) is higher than that of austenite, one can conclude that the ferrite mode of solidification prevails for a given velocity. For details, the reader is referred to prior published works [30, 53]. In this research, the primary mode of solidification was calculated by using these models and was compared with the TRXRD observations.

## *Modeling of Austenite – Martensite Stability in 9Cr welds*

The equilibrium and paraequilibrium thermodynamic phase evolutions were predicted using ThermoCalc® software [43] version P with a solid solution database [44]. By assuming the Scheil–Gulliver additivity law, solidification simulations were performed to evaluate the microsegregation in the as-welded microstructure. Additional calculations were performed to describe the effect of carbon distribution within the austenite during austenitization. Then next set of calculations considered the stability of retained austenite. Diffusion-controlled growth of retained austenite into martensite was evaluated by using DicTra [58, 45] software with a simple geometry and boundary conditions shown in Fig. 4. For these simulations, the Fe-Cr-C alloy system was considered for simplicity. In the first set of calculations, austenite growth with local equilibrium at the interface was assumed. In the second set of calculations, austenite growth with

paraequilibrium considerations was assumed for the same condition given in Fig. 4. MatCalc software [59] was used to calculate the paraequilibrium transformation kinetics.

# Results

## *TRXRD Results from Fe-C-Al-Mn Weld*

TRXRD data from the HAZ region is shown in Fig. 5*a*. In this plot, the diffraction lines appear as dark and the background appears as light. At the start of experiment, the microstructure of the steel is essentially made up of ferrite, and only bcc peaks were present. With the initiation of the arc, the steel heats up and the (110) peaks from the bcc phase move to a lower 2θ angle, indicating the expansion of the lattice. With continued heating, after a certain time, the fcc (111) peaks appeared, and their intensity increased, indicating austenite nucleation and growth. As soon as the arc was extinguished at 17 s, the austenite diffraction peaks decreased, indicating the decomposition of austenite. Careful analysis showed that the austenite peaks did not disappear even after cooling to low temperature, indicating the presence of retained austenite. Peak area analysis [60] is used to convert the TRXRD data into an estimated volume fraction of ferrite. The integrated areas under the fcc (111) and bcc (110) peaks were measured, and the relative phase fraction of ferrite was estimated based on the area fraction of diffraction peaks (see Fig. 5*b*). The data show rapid austenite growth after 6 s into the experiment. Interestingly, the data also show that the ferrite did not transform completely to austenite, indicating the high stability of ferrite in this steel. This is evident in the optical microstructures shown in Fig. 5*c* which shows the presence of coarse δ-ferrite that was originally present in the sample before experiment.

TRXRD results from the rapidly cooled (> 1000 °C/s) FZ region is shown in Fig. 6*a*. The data shown were collected only after extinction of the arc. In the beginning, there is no diffraction from the FZ region, indicating the presence of liquid. At approximately 2 s after arc extinction, the diffraction data showed the emanation of fcc (111) peaks. This indicates that the primary solidification occurred by austenite formation. The fcc (111) peak position moved from a low 2θ angle to a high value with continued cooling. This is related to lattice contraction due to weld cooling. At 4 s from the beginning of measurement, the diffraction peaks from bcc (110) emanated, indicating the decomposition of austenite into low-temperature ferrite or martensite morphologies. Some interesting features of austenite peak splitting were noticed. Optical

microscopy results showed that the final microstructure contained small amounts of bainite and large fractions of martensite. By using integrated peak area analysis, the phase fractions were estimated. The results are shown in Fig. 6*b*. Interestingly, phase fraction analysis showed a slow transformation kinetics (AB) stage and a rapid transformation kinetics (BC) stage. The rate of fraction transformation in the AB stage was 0.334 $s^{-1}$ and 1.40 $s^{-1}$in BC stage. This suggests that there may be more than one form of ferrite morphology. In agreement, the optical microscopy shows the presence of bainite and martensite in the FZ region (see Fig. 6*c*)

TRXRD results from the slowly cooled FZ region (< 100°C/s) is shown in Fig. 7*a*. In this experiment, the data were collected from the FZ, which was cooled slowly by reducing the arc current slowly, over 25 s. Similar to earlier results, no diffraction peaks were observed before the onset of solidification. At ~18 s into the measurement, the bcc (110) diffraction peaks appeared, which is annotated as Ferrite 1, indicating the primary solidification of the ferrite phase. With continued slow cooling, the fcc (111) diffraction peaks appeared briefly, indicating austenite formation. This austenite transformed into ferrite during cooling. Interestingly, the reduction of fcc (111) diffraction peaks coincides with the formation of a secondary bcc (110) diffraction peak, which is annotated as Ferrite 2. The relative phase fractions were estimated based on integrated area analysis. The results are shown in Fig. 7*b*. The optical microstructures (see Fig. 7*c*) from the slowly cooled region are in qualitative agreement with the TRXRD data. The microstructure shows coarse δ-ferrite and austenitic regions in btween the ferrite grains.

## *Phase Transformations in 9Cr Welds*

To evaluate the phase stability of austenite in 9Cr-1Mo-V weld deposits and base metals, samples were subjected to typical normalizing, cooling and tempering treatment. The heat treatment schedules are shown in Fig. 8*a*. The relative radius changes (Δd/d) in both BM and WM samples, as measured by the Gleeble® 3500 during the heat treatment, are presented in Fig. 8*b* and Fig. 8*c* respectively. The transformation temperatures are estimated based on the abrupt slope changes in the plots of relative radius change vs temperature. On heating the base metal above 888°C, contraction was observed due to austenite formation. At 947°C, the dilatometry shows the completion of austenite formation. On cooling from the austenitizing temperature of 1040°C, the decomposition of austenite began at 393°C and appeared to be complete at about 130°C. Subsequently, on heating to 740°C and holding at that temperature, the dilatometry

showed only a small change in the slope, and there was no transformation during cooling from 740°C. The results from the WM sample show similar transformation characteristics except for the temperatures at which these changes took place. The austenite formation during heating occurred at 850°C, and 100% austenite was attained at ~910°C. On cooling from the austenitizing temperature, the decomposition of austenite began at 350°C and appeared to be complete at 100°C. However, while the sample cooled after tempering treatment at 740°C, a secondary martensite reaction at 410°C was observed. This result suggests that there must have been some austenite formation or growth during tempering that transforms to martensite on cooling from tempering temperature.

To evaluate the presence of retained austenite, in situ TRXRD experiments were performed on BM and WM samples while they were being subjected to the same normalizing and tempering treatment shown in Fig. 8*a*. The temperature variations and the diffraction intensities from both BM and WM samples are shown in Fig. 9*a* and 9*b* respectively. Technical difficulties precluded an accurate monitoring of incident X-ray flux, so the diffraction patterns were normalized to a constant total signal; even so, vertical bands are apparent where this normalization was not valid. Gaps in the data correspond to times when X rays were not available. The results from BM [see Fig. 9*a*] show that the austenite γ (200) diffraction peaks disappeared while cooling from the austenitizing temperature. The diffraction peaks disappeared between $1.00 \times 10^4$ and $1.05 \times 10^4$ s. At that time, the sample temperature was between 80°C and 40°C. This suggests that more or less complete transformation of austenite to martensite occurs during normalizing treatment, in agreement with the dilatometric measurements. In contrast, the results from WM [see Fig. 9*b*] show that the austenite γ (200) diffraction peaks are present even after cooling to room temperature. Area fraction analysis of α (200) and γ (200) diffraction peaks indicated an approximate residual austenite percentage of 9 % at room temperature in the WM sample. The diffraction intensities of austenite decreased slightly during the tempering period. The percentage of austenite on heating to 740°C increased slightly to 12%. During isothermal hold at 740°C, the austenite percentage decreased to9 %. In addition to these changes, interestingly, the peak position of austenite γ (200) increased to higher 2θ values. This suggests that there must be an accompanying decrease in austenite lattice parameters. This may be attributed to reduction of solutes and most probably the interstitial elements such as carbon. On cooling from the tempering temperature, the residual austenite transformed to martensite, and no significant

austenite γ (200) peak intensity was observed at room temperature. The above results can be summarized as follows. In the BM samples, the austenite transforms completely to martensite during cooling to room temperature from normalizing temperature. In the WM samples, about 10% of residual austenite remains untransformed at room temperature after cooling from the normalizing temperature. On heating to tempering treatment, the residual austenite possibly reduces its carbon content and becomes less stable, and on cooling it transforms to martensite. These results are in agreement with the trends observed in dilatometric measurements. In the next section, the reasons for such differences in transformation behavior of WM and BM are explored by using computational thermodynamic and kinetic models.

# Discussion

## *Modeling Microstructure Evolution in the HAZ*

Thermodynamic calculations show that the Fe-C-Al-Mn steel used in this research would never transform to 100% austenite on heating [see Fig. 10*a*]. This is in contrast to a Fe-C-Mn steel, in which the room-temperature ferrite-pearlite microstructure transforms to 100% austenite [23]. This observation of incomplete austenite formation is in qualitative agreement with the experimental data shown in Fig. 5. The measured results are compared with the predicted ferrite fraction for two heating cycles (shown in Fig. 10*b* and 10*c*). In this kinetic analysis, the initial microstructure was assumed to be free of cementite, in contrast to the equilibrium predictions shown in Fig. 10*a*. However, it is possible that small amounts of cementite might have precipitated during rapid heating to higher temperature but might not have been tracked by TRXRD because its volume fraction is small. The kinetics of austenite formation was predicted by using diffusion-controlled growth models for the conditions described earlier. Simulations with one-stage heating to a peak temperature of 1733 K [see Fig. 10*c*] lead to an interesting result. Initially, the austenite forms and grows rapidly into the ferrite. However, above 1580 K, the reverse transformation of the austenite to δ-ferrite is predicted. This is related to increased stability of δ-ferrite at high temperature. In contrast, the two-stage heating leads to continued growth of austenite into ferrite, and the ferrite fraction reduces to 42%. This prediction is in qualitative agreement with the experimentally observed reduction in the ferrite fraction.

The trends observed in the experiments generally agree with the predictions, except that the reduction of ferrite to 30% in the experiments is lower than the predicted value of 42%. This discrepancy is attributed to the temperature gradient within the measurement volume in the HAZ as well as the simplistic geometry and heating cycle used in the simulation. In real welds, the above scenario will be complicated by the following phenomena: (1) the rapid tempering of martensite leads to presence of cementite and ferrite, which will reduce the austenite formation kinetics at the early stages, and (2) the nucleation of austenite may not readily occur as assumed in these calculations. An increased barrier for nucleation of austenite will also lead to sluggish austenite formation kinetics. . The focus of ongoing research is to understand the spatial variation of peak temperatures, rate of heating, and the change of transformation mode from diffusion-controlled transformation to possible massive transformation of ferrite to austenite.

## *Modeling Phase Selection in the FZ*

The calculated ferrite fractions given in Fig. 10*a* show that the primary solidification in these alloys should be δ-ferrite. In agreement with predictions, the welds under normal cooling conditions exhibit a columnar δ-ferrite microstructure [35]. On the other hand, the TRXRD results from the rapidly cooled FZ indicated primary austenite solidification (see Fig. 6*b*). This transition from δ-ferrite to austenite solidification is attributed to a rapid increase in the liquid-solid interface velocity brought about by the high cooling rate experienced during the TRXRD experiments. The TRXRD results from spot welds with a reduced cooling rate showed that the equilibrium δ-ferrite solidification can be restored (see Fig. 7*b*).

Similar changes in solidification mode from ferrite to austenite have been observed in rapidly cooled stainless steel welds as determined by post-weld characterization. However, in the current alloy, such changes cannot be inferred from post-weld microstructures due to the destruction of the solidification microstructure by solid-state transformations. The observation of bainitic ferrite and martensite in the FZ at room temperature does not present any clues about solidification microstructure. The results from optical microscopy (see Fig. 6*c*) alone are ambiguous, giving two possible mechanisms for the evolution of the microstructure:

$$Liquid \Rightarrow \delta - ferrite \Rightarrow austenite\ by\ massive\ transformation \Rightarrow bainite + martensite \qquad \text{(I)}$$

*Liquid ⇒ austenite by nonequilibrium solidification ⇒ bainite + martensite* (II)

The TRXRD results showed that in these welds sequence II is the operating mechanism, whereby the weld solidifies directly to the nonequilibrium austenite phase before transforming to bainite and martensite. Such phase selection in weld solidification can be evaluated by using interface-response function models. These models have been successfully applied to predict nonequilibrium austenite formation in stainless steel welds. By using this model, the liquid-δ-ferrite interface and liquid-austenite interface temperatures can be estimated as a function of interface velocity. If the temperature of the liquid-δ-ferrite interface is higher than that of the liquid-austenite interface, one can conclude that the liquid-δ-ferrite will lie ahead of the liquid - austenite interface. In other words, this will suggest a primary mode of solidification by δ-ferrite. The opposite will be true for the primary mode of solidification by austenite. The same methodology was extended to the present steel.

Thermodynamic parameters for the model were calculated by using ThermoCalc® software [43]. The results based on the published [30] Gibbs-Thompson coefficient (Γ) for steels are shown in Fig. 11*a*. The results show that the liquid–δ-ferrite interface temperatures for the dendritic mode of solidification are always higher than that of the liquid –austenite interface. The expected velocity ranges for the present welding conditions are also shown in Fig. 11*a*. The calculations show that the transition to the austenite mode of solidification is not expected. This prediction is contrary to the experimental observation. Additional calculations were made to assess the sensitivity of the results to the Gibbs - Thompson coefficient, Γ. By arbitrarily changing the value of Γ for ferrite from $2.6 \times 10^{-7}$ to $2.6 \times 10^{-6}$, the interface temperature could be reduced to a temperature below that of austenite. With these new calculations [see Fig. 11*b*], the austenite dendrite-tip interface would lie ahead of the ferrite dendrite-tip interface, resulting in an austenitic mode of solidification. This is in agreement with experimental observations. Furthermore, at lower velocities, the δ-ferrite solidification would prevail, as found experimentally in slowly cooled spot welds (see Fig. 7*b*).

Although this finding is in agreement with experimental measurement, future work is needed to rationalize the selection of an appropriate Gibbs Thompson coefficient (Γ). The value of Γ is related to the ratio of interfacial energy (σ) and the entropy change ($\Delta S_f$) on melting per unit

volume [61, 62]. This suggests that the σ of the liquid-δ-ferrite interface must be higher than that of the liquid-γ-austenite interface during rapid cooling conditions. Arnold et al. [62] addressed the calculation of σ based on the model of Spaepen [63]. Spaepen's model relates the σ to $\Delta S_f$ and type of crystal structure for a monoatomic system. However, these models do not consider the effect of solute trapping on the interfacial energy. Carbon trapping may therefore play an important role in ferrite solidification. Further work is under way to derive these values as a function of a velocity-dependent partitioning coefficient.

## *Modeling the Microstructure Evolution in 9Cr Welds*

The main differences between the WM and BM samples in 9Cr alloys are small differences in composition [see Table I] and the preprocessing. The BM samples have been subjected to repeated-solutionizing and high-temperature deformation, which in turn destroys the original as-cast microstructure. In contrast, the WM samples have not been subjected to extensive solutionizing, except for repeated thermal cycling of multipass welding and PWHT. As a result, the WM samples are expected to have large microsegregation of alloying elements. These microsegregation patterns may locally change the transformation characteristics and may lead to the observed microstructural evolution. This hypothesis was evaluated with systematic thermodynamic and kinetic calculations in this section.

To evaluate the segregation patterns in the as-welded microstructure, the solidification simulation was performed by assuming Scheil-Gulliver method [64, 65]. The above simulations did not consider the back-diffusion of elements and used the solid solution database and ThermoCalc® software [43]. The calculations with WM compositions showed that the first phase to solidify is δ-ferrite. Toward the end of solidification (> 90% solid), interdendritic regions are enriched with alloying elements, especially carbon and nitrogen. This enrichment leads to a prediction of austenite formation at the interdendritic regions toward the end of solidification. The variation of chromium and carbon in the solid phase predicted by the Scheil-Gulliver method is shown in Fig. 12*a*. The calculations show that typical chromium variation from the intradendritic region to interdendritic region may vary from 8.9 to 11.3 wt % Cr and may undergo a corresponding carbon variation from 0.02 to 0.4 wt %. Although these segregation ranges may decrease slightly during repeated thermal cycling of multipass welds and some PWHT temperature, they cannot be eliminated due to limited time allowed at high

temperature. The microstructure of the weld deposit is shown in Fig. 12*b*, where tint etching was used to reveal the microsegregation pattern that is normally obscured by common etching techniques. This pattern has a spacing of 50 to 100 μm, which is consistent with the dendrite arm spacing expected in submerged-arc steel welds [66].

Although one can expect the microsegregation to play an important role in phase transformation, there is a need to rationalize the incomplete austenite to martensite transformation in WM samples during cooling from 1040°C. This was evaluated with Fe-Cr-C system for simplicity. Thermodynamic calculations in a Fe-Cr-C system showed that on heating to 1040°C the as-welded microstructure should transform completely to austenite. The calculations showed that 100% austenite would be formed at this temperature even with chromium segregation present in the interdendritic region. Additional calculations showed that the effect of chromium segregation might lead to a small carbon concentration gradient (0.09 wt % C at 8.8 wt % Cr to 0.12 wt % C at 11.9 wt % Cr) to satisfy the isoactivity condition for carbon at this austenitization temperature. This implies that during austenitization at 1040° C, the most mobile carbon atom may reach its isoactivity level by diffusing fast and will set up a concentration gradient across the dendritic core and interdendritic regions. It is noteworthy that this spatial variation of carbon and chromium will lead to regions with different martensite start temperatures ($M_s$). The $M_s$ for Fe-Cr-C system was predicted by using a model developed by Ghosh and Olson [67]. The calculated $M_s$ for the dendritic core region (0.09 wt % C at 8.8 wt % Cr) was 416°C. The calculated $M_s$ for interdendritic region was found to be 357°C. These calculations show that the WM regions would show a large temperature range over which the transformation from austenite to martensite may occur. This is in agreement with the trends observed in the present investigation. These calculations could be extended to other alloying additions and were not done in the present investigation. The same trends can also be explained by the empirical equation that describes the martensite start temperature as a function of alloy concentrations in weight percent.

$$M_s(°C) = 454 - 210 \times C \ - 4.2/C - 27 \times Ni - 7.8 \times Mn - 9.5 \times \left[Cr + Mo + V + W + 1.5 * Si\right] \qquad (6)$$

The equation was evaluated for a range of carbon and chromium concentrations. The results show that for the predicted concentration variations within a single dendrite, the $M_s$ temperature

may vary from 320 to 280°C. These calculations were also repeated for the nominal BM composition and WM compositions [see Table 1]. The results showed that the predicted $M_s$ temperature is 383°C for BM and is 347°C for WM. The dilatometric measurements showed 393°C for BM and 350°C for WM samples. In the literature, the martensite finish temperature is assumed to be 200°C below that of $M_s$ temperature. However, the current TRXRD measurements show that the austenite to martensite transformation is not complete in the WM at that temperature. This is assumed to be due to the presence of other alloying elements (including nitrogen) that are not considered in the analysis of solidification segregation and subsequent austenitization. Nevertheless, the above calculations support the observed difference in the martensite start temperature in the BM and WM samples.

Previous calculations rationalized the changes in $M_s$ temperature between BM and WM samples, but not the stability of the residual austenite at tempering temperature (740°C). The equilibrium calculations for a Fe-Cr-C system at 740°C showed that the austenite is highly unstable and should decompose to α-ferrite and $M_{23}C_6$ carbide [see Fig. 13*a*]. Both TRXRD and dilatometric measurements from WM showed the presence of austenite and changes to austenite during tempering at 740°C. Since carbide formation usually takes incubation time, the next set of calculations were done by ignoring the carbides in the equilibrium. This leads a quasi-equilibrium phase diagram between ferrite and austenite as shown in Fig. 13*b*. The phase boundaries were calculated by considering both substitutional and interstitial element partitioning (i.e., local equilibrium). In addition, calculations were repeated by assuming only a carbon partition (i.e., paraequilibrium) [68]. Both the calculations support that a metastable equilibrium between austenite and ferrite may be possible at 740°C. It is speculated that on heating to tempering temperature metastable phase equilibrium occurs and leads to a reduction in austenite carbon. As a result, this austenite might now transform to martensite on cooling.

The previous calculations showed that there may exist a metastable equilibrium between austenite and ferrite at 740°C. However, the consequence of this equilibrium based on the microstructure present after normalizing treatment was not predicted. To evaluate this, the diffusion-controlled growth of austenite into martensite (ferrite) at 740°C was simulated. These calculations considered the boundary conditions shown in Fig. 4. All the boundary conditions used are typical and may not correspond to conditions that exist after the cool down to room temperature from 1040°C. The calculations were performed under two conditions: (1) assuming

local equilibrium [58] and (2) assuming paraequilibrium [69]. Under local equilibrium conditions, the condition leads to steep concentration profile.

Both the calculations showed that there would be rapid growth of austenite within 3 min of isothermal holding at 740°C (see Fig. 14). However, the paraequilibrium conditions lead to higher fractions of austenite. The growth of austenite appears to support the observed secondary martensite formation while cooling from tempering temperature. However, detailed analysis showed that the predicted austenite carbon concentration after isothermal holding at 740°C for 15 min does not lead to a drastic change in the carbon concentration. This is in contradiction to the observed higher secondary martensite start temperature. It is highly possible that on heating to 740°C, the carbon content of the martensite may be reduced due to paraequilibrium cementite formation. This reduction in carbon may then lead to decomposition of austenite to martensite at higher temperature than the original $M_s$ temperature of the weld. Therefore, further work is necessary to describe the stability of austenite with respect to paraequilibrium carbide (cementite) formation [70].

## Summary and Conclusions

The transition from equilibrium to nonequilibrium microstructure is an inherent part of weld microstructure evolution, and the present paper describes this phenomenon in a Fe-C-Al-Mn and 9Cr-1Mo-V steel.

The growth of austenite during weld heating was characterized by using TRXRD in Fe-C-Al-Mn steel welds. An incomplete austenitization in the HAZ occurred because of increased phase stability of ferrite caused by a large (> 1 wt %) aluminum concentration. This microstructure was in qualitative agreement with computational thermodynamic and kinetic calculations and stressed the importance of predicting accurate thermal cycles.

During rapid cooling, TRXRD was used to observe the transition from equilibrium δ-ferrite to austenite in the FZ of Fe-C-Al-Mn steel welds. With the same technique, the formation of equilibrium δ-ferrite during slow cooling was monitored. The changes in the primary mode of solidification with the change in cooling rate were evaluated by coupling interface response function models with thermodynamic calculations. The calculations with published thermodynamic parameters showed that primary austenite solidification is not expected and that

ferrite primary solidification should occur. An analysis of the model showed that the predictions are very sensitive to the assumed Gibbs Thompson interface coefficient. Adjustments in this parameter lead to predictions in agreement with the experimental observations.

The phase transformations in the 9Cr-1Mo-V WM region were compared with that of the BM by using dilatometry and TRXRD. Dilatometry indicated a secondary martensite reaction during cooling from tempering treatment in the WM samples; this secondary reaction was absent in the BM samples. This phenomenon is related to the stability of untransformed austenite in the WM regions. The above hypothesis was in agreement with TRXRD results. Computational thermodynamic calculations related this phenomenon to the solidification segregation and to the depression of the martensite transformation temperature in these regions. Additional calculations suggest possible modification of the austenite solute content during PWHT by growth of austenite content. This modification may lead to decomposition to martensite during cooling from PWHT.

## Acknowledgments

The research was sponsored by the U.S. Department of Energy Division of Materials Sciences and Engineering (TRXRD investigations at SSRL), Office of Energy Efficiency and Renewable Energy, Industrial Technologies Program, Industrial Materials for the Future (TRXRD investigations at APS), Office of Fossil Energy, U.S. Department of Energy, National Energy Technology Laboratory (Dilatometry investigation on 9Cr-1Mo-V welds) under contract No. DE-AC05-00OR22725 with UT-Battelle, LLC. A portion of this work (TRXRD investigations at SSRL) was performed under the auspices of the U. S. Department of Energy, Lawrence Livermore National Laboratory, under Contract No. W-7405-ENG-48. The UNICAT facility at the Advanced Photon Source (APS) is supported by the University of Illinois at Urbana-Champaign, Materials Research Laboratory (U.S. DOE, the State of Illinois-IBHE-HECA, and the NSF), the Oak Ridge National Laboratory (U.S. DOE under contract with UT-Battelle LLC), the National Institute of Standards and Technology (U.S. Department of Commerce) and UOP LLC. The APS is supported by the U.S. DOE, Basic Energy Sciences, Office of Science under contract No. W-31-109-ENG-38. Some portions of research were carried out at the Stanford Synchrotron Research Facility, a national user facility operated by Stanford University on behalf of the U. S. Department of Energy, Office of Basic Energy Sciences.

The authors would like to thank Drs. Joe Wang and T. A. Palmer of LLNL for help with the synchrotron diffraction experiments, Ms. M. A. Quintana of Lincoln Electric, Cleveland, Ohio for providing welds, Dr. G. Ghosh and Prof. G. B. Olson of Northwestern University for providing us the macro files to calculate martensite start temperature in Fe-Cr-C system and the encouragement of and helpful discussions with Bill Newell of Euroweld, Ltd. are greatly appreciated. The assistance with metallographic specimen etching provided by George VanderVoort of Buehler Ltd. was invaluable. The authors would like to thank Drs Z. Feng and M. Murugananth for reviewing the manuscript.

## References

1. Welding Handbook, "Welding Technology," Volume 1, 8th edition, Page 111, American Welding Society, Editor L. P. Connor, 1987.
2. S. A. David, T. DebRoy, and J. M. Vitek, "Phenomenological modeling of fusion welding processes, *MRS Bulletin*, **19**, 29-35, (1994)
3. S. A. David and T. DebRoy, "Current issues and problems in welding science," *Science*, **257**, 497-502, (1992)
4. T. W. Eagar, "Physics of Arc Welding," *AIP Conference Proceedings*, **84**, 272-285 (1982)
5. L. A. Jones, T. W. Eagar, and J. H. Lang, "A dynamic model of drops detaching from a gas metal arc welding electrode," *J. Phys. D: Appl. Phys*., **31**, 107-123, (1998).
6. H. Ki, P. S. Mohanty, and J. S. Mazumder, "Modeling of laser keyhole welding: Part I. Mathematical modeling, numerical methodology, role of recoil pressure, multiple reflections, and free surface evolution," *Metall. Mater. Trans. A*, **33**, 1817-1830, (2002)
7. H. Ki, P. S. Mohanty, and J. S. Mazumder, "Modeling of laser keyhole welding: Part II. Simulation of keyhole evolution, velocity, temperature profile, and experimental verification," *Metall. Mater. Trans. A*, **33**, 1817-1830, (2002)
8. U. Dilthey, A. Goumeniouk, V. Lopota, G. Turichin, E. Valdaitseva, "Development of a theory for alloying element losses during laser beam welding," *Journal of Physics D – Applied Physics*, **34**, 81-86, (2001)

9. J. Goldak, A. Chakravari and M. Bibby, "A New finite-element model for welding heat sources," *Metall. Trans. B – Process Metallurgy*, **15**, 299-305, 1984

10. T. Zacharia, A. H. Eraslan, D. K. Aidun and S. A. David, "3-Dimensional transient model for arc welding process," *Metall. Trans. B – Process Metallurgy*, **20**, 645-659, 1989.

11. Y. Hirata, Y. Asai, K. Takenaka, S. Ohgaki, F. Miyasaka and T. Ohji, "3D-numerical model predicting penetration shape in gta welding," Thermec'2003, PTS 1-5, *Materials Science Forum*, **426-4**, 4045-4050, (2003)

12. K. Mundra, T. DebRoy and K. M. Kelkar, "Numerical prediction of fluid flow and heat transfer in welding with a moving heat source," *Numerical Heat Transfer Part A – Applications*, **29**, 115-129, (1996)

13. T. Debroy, and S. A. David, "Physical Process in Fusion Welding," *Reviews of Modern Physics*, **67**, 85-112, (1995)

14. U. Mitra and T. W. Eagar, "Slag metal reactions during welding. 2. Theory," *Metall. Trans. B*., **22**, 73-831, (1991)

15. S. Liu, "Recent Approaches in the Deisgn of Flux-related Arc Welding Consumables," *Mathematical Modeling of Weld Phenomena – 5*, Edited by H. Cerjak, Materials Modeling Series, Institute of Materials, 2001.

16. P. S. Mohanty and J. Mazumder, "Solidification behaviour and microstructural evolution during laser beam-material interaction," *Metall. Mater. Trans. B.,* **29**, 1269-1279, (1998)

17. S. A. David, S. S. Babu and J. M. Vitek, "Welding: Solidification and Microstructure," *JOM-Journal of the Minerals Metals and Materials Society*, **55**, 14-20, (2003)

18. S. A. David and J. M. Vitek, "Correlation between solidification parameters and weld microstructures," *Int. Materials Review*, **34**, 213-245, (1989)

19. M. Rappaz, S. A. David, J. M. Vitek, "Analysis of solidification microstructures in Fe-Ni-Cr single-crystal welds," *Metall. Trans. A.* **21**, 1767-1782, (1990).

20. K. E. Easterling, "Solidification microstructure of fusion welds," *Materials Science and Engineering*, **65**, 191-198, (1984)

21. M. F. Ashby and K. E. Easterling, "A 1st report on diagrams for grain growth in welds," *Acta. Metall. Mater.*, **30**, 1969-1978, (1982)

22. H. K. D. H. Bhadeshia, L. –E. Svensson and B. Gretoft, "A model for the development of microstructure in low-alloy steels (Fe-Mn-Si-C) weld depositions, *Acta Metall. Mater.*, **33**, 1271-1283, (1985)

23. J. W. Elmer, T. A. Palmer, W. Zhang, B. Wood, and T. DebRoy, "Kinetic Modeling of Phase Transformations Occurring in the HAZ of C-Mn Steel Welds Based on Direct Observations," in press *Acta Materialia*, 2003, **51**, 3333-3349.

24. P. Dong and F. W. Brust, "Welding residual stresses and effects on fracture in pressure vessel and piping components: A millennium review and beyond," *Journal of Pressure Vessel Technology-Transactions of the ASME*, **122**, 329-338, (2000)

25. J. M. J. McDill, A. S. Oddy, J. A. Goldak, and S. Bennison, "Finite-element analysis of weld distortion in carbon and stainless-steels," *J. of Strain Analysis for Engineering Design*, **25**, 51-53, (1990)

26. K. Masubuchi, "Investigation of methods controlling and reducing weld distortion in aluminum structures," *Weld. Res. Council Bullettin,* **237**, 1-27, (1978)

27. J. X. Zhang, Y. W. Shi and H. Murakawa, "The study on ductile fracture of the over-matched weldment with mechanical heterogeneity," *Int. J. of Pressure Vessels and Piping*, **75**, 773-776 (1998)

28. Z. Feng, S. A. David, T. Zacharia, C. L. Tsai, "Quantification of thermomechanical conditions for weld solidification cracking," *Sci. Technol. Welding and Joining*, **2**, 11-19, (1997)

29. D. Dye, O. Hunziker, S. M. Roberts and R. C. Reed, "Modeling the mechanical effects induced by the tungsten inert-gas welding of the IN718 superalloy," *Metall. Mater. Trans. A*., **32**, 1713-1725, (2001).

30. S. Fukumoto and W. Kurz, "Prediction of the delta to gamma transition in austenitic stainless steels during laser treatment," *ISIJ International*, **38**, 71-77 (1998)

31. J. M. Vitek, S. A. Vitek, and S. A. David, "Numerical modeling of diffusion-controlled phase transformations in ternary-systems and application to the ferrite-austenite transformation in the Fe-Cr-Ni system," *Metall. Mater. Trans. A*., **26**, 2007-2025, (1995)

32. J. M. Race and H. K. D. H. Bhadeshia, "Precipitation sequences during carburaization of Cr-Mo steel," *Materials Science and Technology*, **8**, 875-882, (1992)

33. E. Kozeschnik, P. Polt, S. Brett and B. Buchmayr, "Dissimilar 2.25Cr/9Cr and 2Cr/0.5CrMoV steel welds – Part 1: Characterization of weld zone and numerical simulation," *Scienc and Technology of Welding and Joining*, **7**, 65-68, (2002)

34. J. M. Vitek, E. Kozeschnik, S. A. David, "Simulating the ferrite-to-austenite transformation in stainless steel welds," *CALPHAD*, **25**, 217-230, (2001)

35 . S. S. Babu, S. A. David and M. A. Quintana, "Modeling microstructure evolution in self-shielded flux-cored arc welds," *Welding Journal*, **80**, 91s-105s (2001)

36. M. A. Quintana, J. McLane, S. S. Babu, S. A. David, "Inclusion formation in self-shielded flux-cored arc welds," *Welding journal*, **80**, 98s-105s (2001)

37. F. V. Ellis, J. F. Henry, and B. W. Roberts, "Welding, Fabrication, and Service Experience with Modified 9Cr-1Mo Steel," pp. 55-63 in New Alloys for Pressure Vessels and Piping, PVP Volume 201, American Society of Mechanical Engineers, NY, 1990.

38. T. Wada, *The Continuous Cooling Transformation Diagram and Tempering Response of 9Cr-1Mo-V-Nb Steels*, J-4672, Climax Molybdenum Company of Michigan, Ann Arbor, MI, 1981.

39. V. K. Sikka, C. T. Ward, and K. C. Thomas, "Modified 9Cr-1Mo Steel – An Improved Alloy for Steam Generator Application," pp. 65-84 in *Ferritic Steels for High-Temperature Applications*, edited by A. K. Khare, American Society for Metals, Metals Park, OH, 1983.

40. G. C. Bodine, C. Chakravarti, C. M. Owens, B. W. Roberts, D. M. Vandergriff, and C. T. Ward, *A Program for the Development of Advanced Ferritic Alloys for LMFBR Structural Application*, ORNL/Sub-4291/1, TR-MCD-015, Oak Ridge National Laboratory, 1977.

41. W. Zhang, G. G. Roy, J. W. Elmer and T. DebRoy, "Modeling of heat transfer and fluid flow during gas tungsten arc spot welding of low carbon steel," *J. Applied Physics*, **93**, 3022-3033 (2003)

42. V. Karpenko, J. H. Kinney, S. Kulkarni, K. Neufel, C. Pope, K. G. Tirsell, J. Wong, J. Cernio, T. Troxel, and J. Yang, "Beamline-10 - a multipole wiggler beamline at SSRL," *Review of Scientific Instruments*, **60**, 1451, (1989)

43. B. Sundman, B. Jansson, and J. O. Andersson, "The thermo-calc databank system," *Calphad*, **9**, 1-153, (1985)

44. SGTE Solution Database (1992) Editor: B. Sundman, Division of Computational Thermodynamics, Royal Institute of Technology, Stockholm, Sweden.

45. A. Borgenstam, A. Engstrom, L. Hoglund, J. Agren, "DICTRA, a tool for simulation of diffusional transformations in alloys," *J. Phase Equilibria*, **21**, 269-280, (2000)

46. S. S. Babu, unpublished research, Oak Ridge National Laboratory, Oak Ridge, TN 37831-6096 (2003)

47. W. Kurz, B. Giovanola, and R. Trivedi, "Theory of microstructural development during rapid solidification," *Acta Metall*, **34**, 823-830, (1986)

48. M. J. Aziz, Model for solute distribution during rapid solidification, *J. Appl. Physics*, **53**, 1158-1168, (1982)

49. O. Hunziker, "Theory of plane front and dendritic growth in multicomponent alloys," *Acta Mater*., **49**, 4191-4203, (2001)

50. N. Suutala, "Effect of solidification conditions in the solidification model in austenitic stainless steels," *Metall. Trans. A.*, **14A**, 191-197, (1983)

51. R. Trivedi and W. Kurz, "Dendritic growth," *International Materials Reviews*, **39**, 49-74, (1994)

52. O. Hunziker, M. Vandyoussefi and W. Kurz, "Phase and microstructure selection in peritectic alloys close to the limit of constitutional undercooling," *Acta Mater*, **46**, 6325-6336 (1998)

53. S. S. Babu, J. W. Elmer, J. M. Vitek and S. A. David, "Time-resolved X-ray diffraction investigation of primary weld solidification in Fe-C-Al-Mn steel welds," *Acta Mater*, **50**, 4763-4781, (2002)

54. M. Rappaz, S. A. David, J. M. Vitek and L. A. Boatner: "Analysis of Solidfication Microstructures in Fe-Ni-Cr Single-Crystal Welds," *Metall Trans A*, **21A**, 1767-1782 (1990).

55. S. Fukumoto and W. Kurz, "Solidification phase and microstructure selection maps for Fe-Cr-Ni alloys," *ISIJ International,* **39**, 1270-1279, (1999)

56. S. Fukumoto and W. Kurz, "The δ to γ transition in Fe-Cr-Ni alloys during laser treatment," *ISIJ International,* **37**, 677-684, (1997)

57. W. Kurz and D. J. Fisher, Fundamentals of Solidification, Fourth Revised Edition, Trans Tech Publications Ltd, USA, 1998, Page 242.

58. J.-O. Andersson, L. Höglund, B. Jönsson and J. Ågren, "Computer Simulation of Multicomponent Diffusional Transformations in Steel," *Fundamentals and Applications of Ternary Diffusion*, ed. G. R. Purdy (New York, NY: Pergamon Press, 1990), 153-163.

59. E. Kozeschnik and B. Buchmayr, "MatCalc – A simulation tool for multicomponent thermodynamics, Diffusion and Phase Transformation Kinetics," *Mathematical Modeling of Weld Phenomena 5*, ed. H. Cerjak (London: Inst. Of Materials, 2001), 349-361

60. T. A. Palmer, J. W. Elmer, and Joe Wong, "In situ Observations of Ferrite/Austenite Transformations in Duplex Stainless Steel Weldments Using Synchrotron Radiation," *Science and Technology of Welding and Joining*, **7**,159-171, (2002)

61. R. Trivedi and W. Kurz, "Dendritic Growth," *International Materials Reviews*, **39**, 49-74, (1994)

62. C. B. Arnold, M. J. Aziz, M. Schwarz, and D. M. Herlach, "Parameter-free test of alloy dendrite-growth theory," *Physical Review B*, **59**, 334-343, (1999)

63. F. Spaepen, "A structural model for the solid-liquid interface in monoatomic systems," *Acta Metallurgica*, **23**, 729-743, (1975).

64. H. D. Brody and M. C. Flemings, "Solute redistribution in dendritic solidification," *Trans. Met. Soc, AIME*, **236**, 615-623, (1966)

65. E. Kozeschnik, "A Scheil-Gulliver model with back-diffusion applied to the microsegregation of chromium in Fe-Cr-C alloys," *Metall. Mater. Transactions A*., **31**, 1682-1684, (2000)

66. S. A. David and J. M. Vitek, "Correlation between solidification parameters and weld microstructures," *International Materials Reviews*, **35**, 213-245, (1989).

67. G. Ghosh and G. B. Olson, "Kinetics of FCC->BCC Heterogeneous martensitic nucleation – 1. The critical driving force for athermal nucleation," *Acta Metall. Mater.*, **42**, 3361-3370, (1994)

68. M. Hillert, “Nature of local equilibrium at the interface in the growth of ferrite from alloyed austenite,” *Scripta Materialia*, **46**, 447-453, (2002)

69. E. Kozeschnik and J. M. Vitek, “Ortho-equilibrium and para-equilibrium phase diagrams for interstitital/substitutional iron alloys,” *CALPHAD*, **24**, 495-502, (2000)

70. S. S. Babu, K. Hono, and T. Sakurai, “Atom-probe field-ion microscopy study of the partitioning of substitutional elements during tempering of a low-alloy steel martensite,” *Metall. Mater. Trans. A.*, **25**, 499-508, (1994)

## Figure Captions

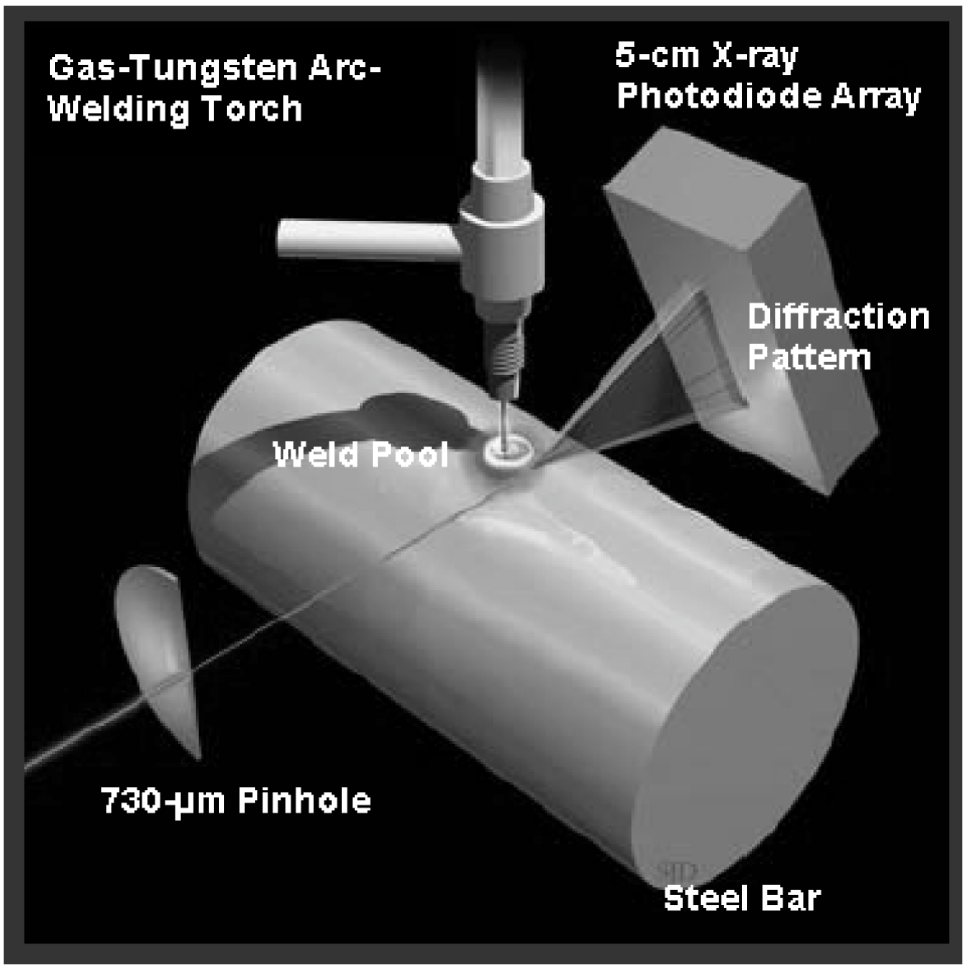


Fig. 1 Schematic illustration of the X-ray diffraction and welding set up used in the present research to study nonequilibrium phase formation in Fe-C-Al-Mn spot welds.

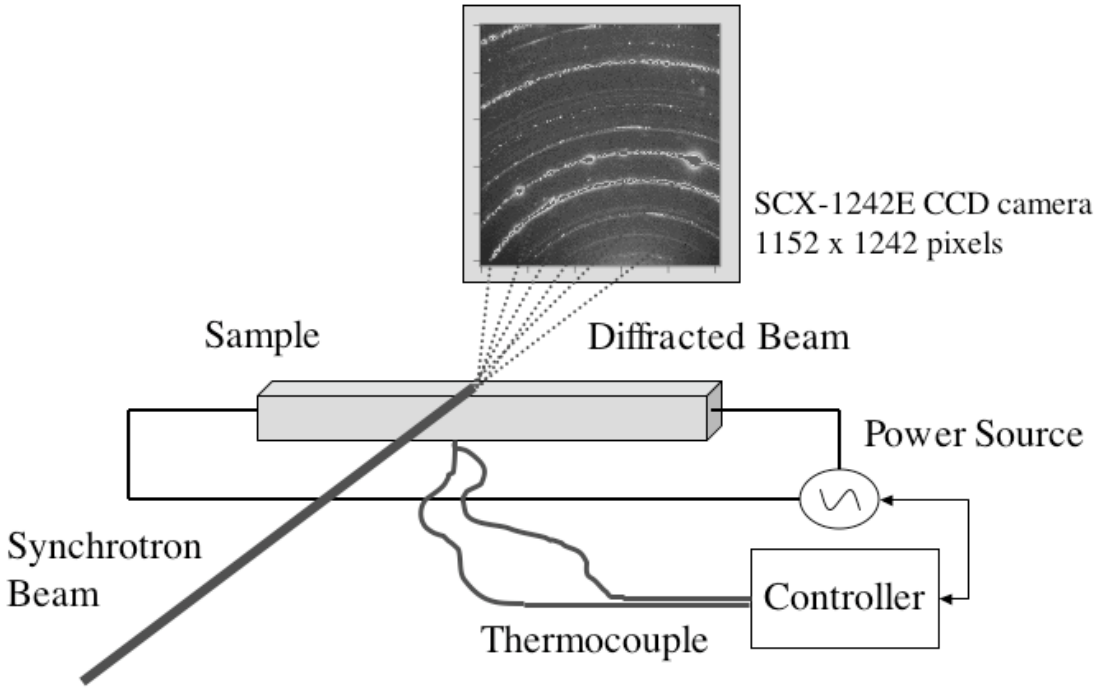


Fig. 2 Schematic illustration of the X-ray diffraction and sample heating setup used for studying the residual austenite stability in 9Cr-1Mo-V steel welds. The illustration does not show the sample chamber that was dynamically purged with helium and aluminum foil that filters the fluorescence.

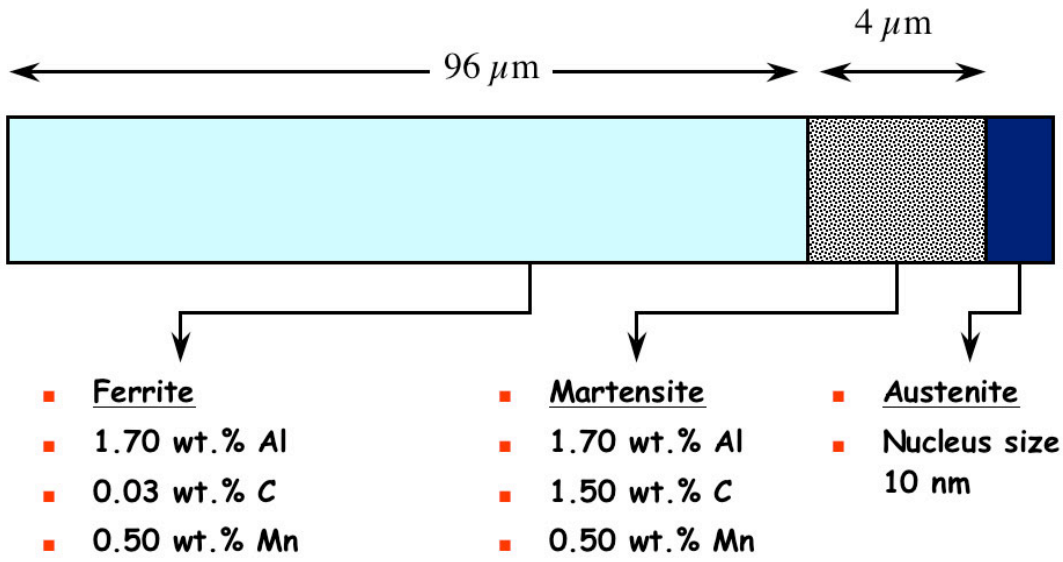


Fig. 3 Schematic illustration of the simulation geometry and boundary conditions used in diffusion controlled calculation of austenite formation and growth in the HAZ of the weld.

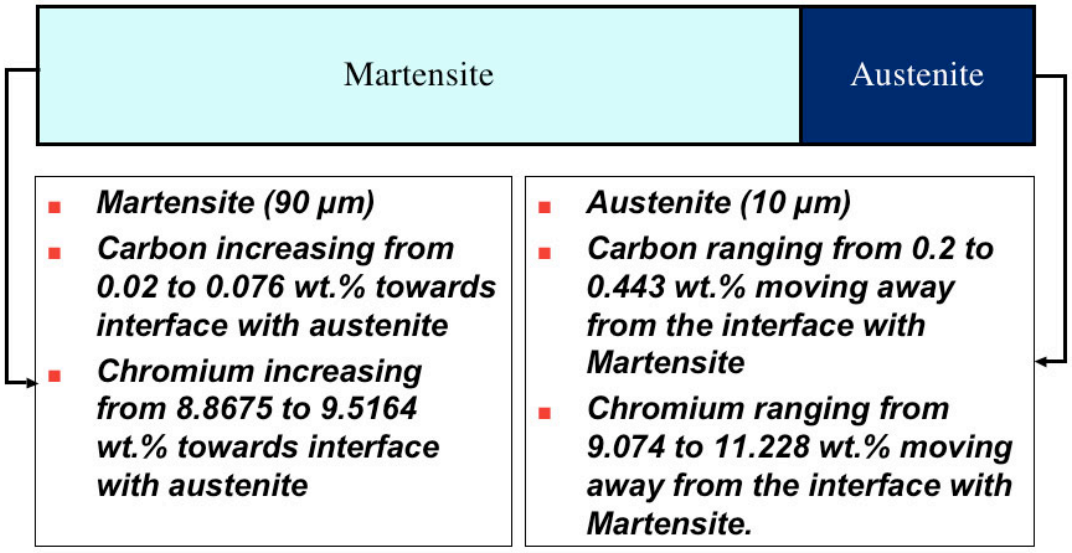


Fig. 4 Boundary conditions and geometry used for simulating the stability of austenite during tempering at 740 °C in a Fe-Cr-C system.

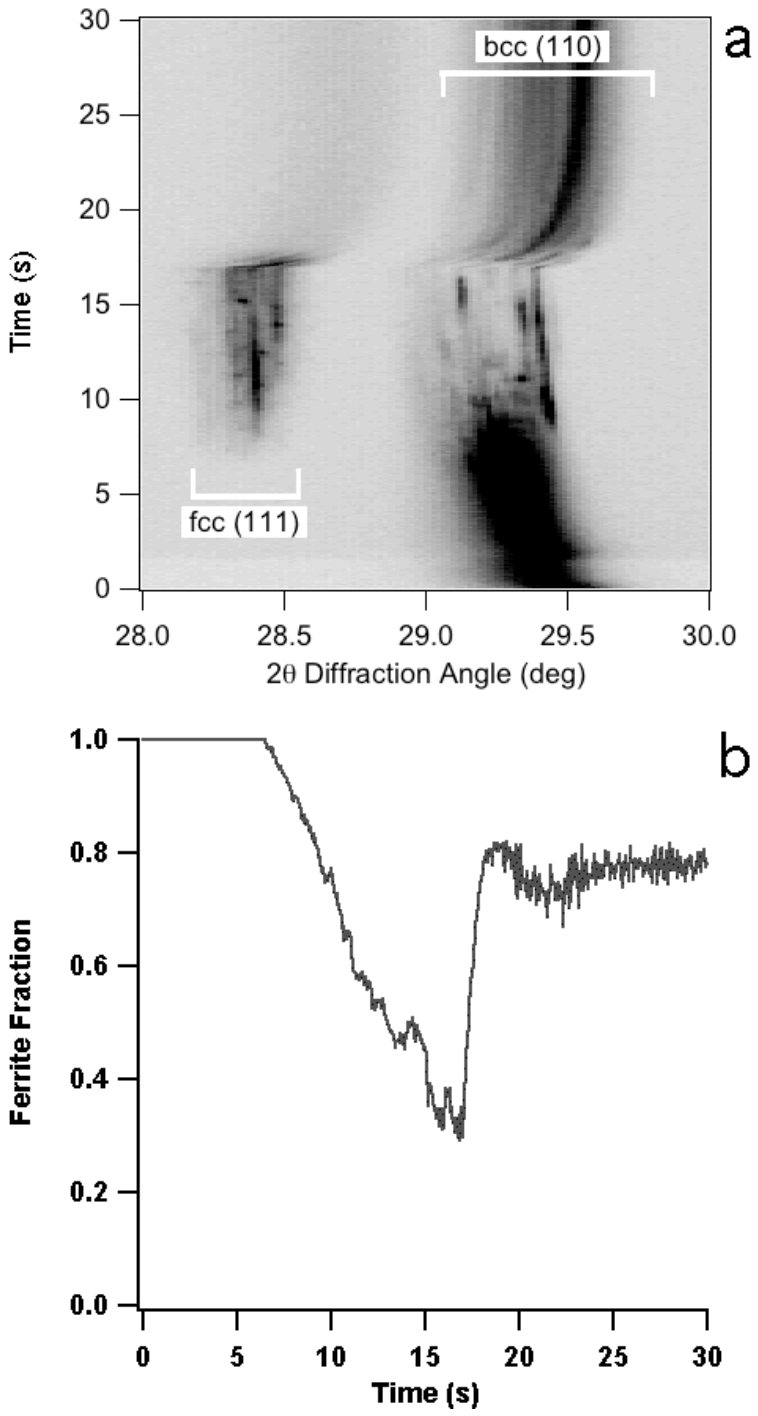
a
bcc (110)
fcc (111)
Time (s)
2θ Diffraction Angle (deg)
b
Ferrite Fraction
Time (s)

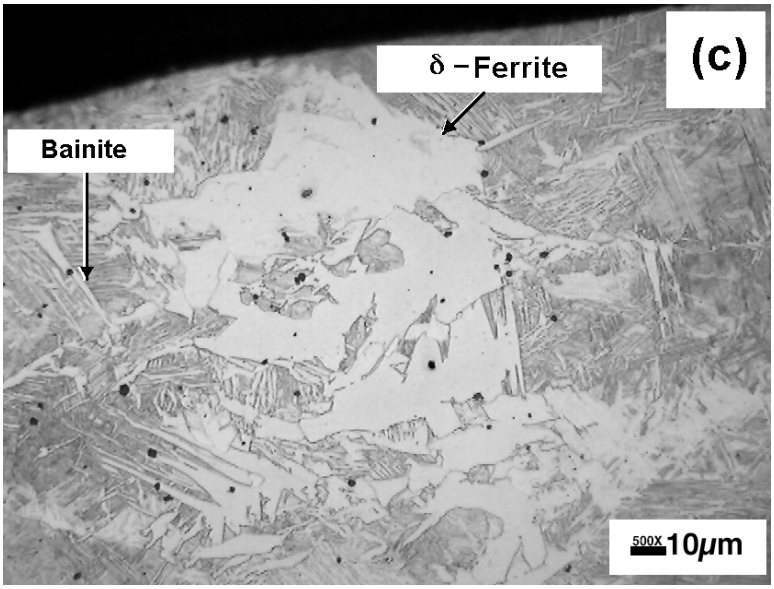


Fig. 5 (*a*) TRXRD data from the HAZ region of Fe-C-Al-Mn spot weld is shown in image format. (*b*) Calculated ferrite fraction based on integrated area fraction shows the incomplete austenite formation. (*c*) Optical micrograph shows the original coarse δ-ferrite and bainite that forms from the austenite.

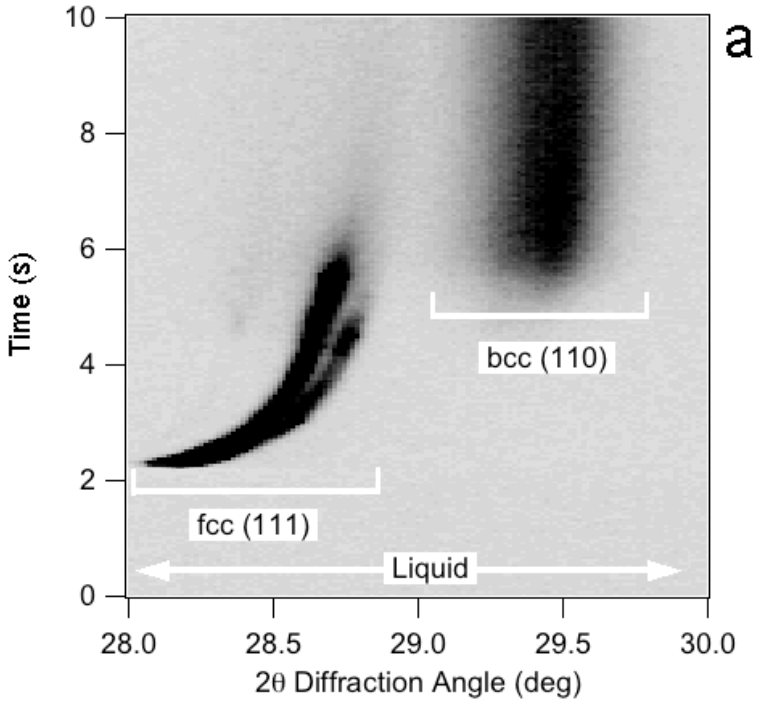
a
Time (s)
10
8
6
4
2
0
bcc (110)
fcc (111)
Liquid
28.0
28.5
29.0
29.5
30.0
2θ Diffraction Angle (deg)

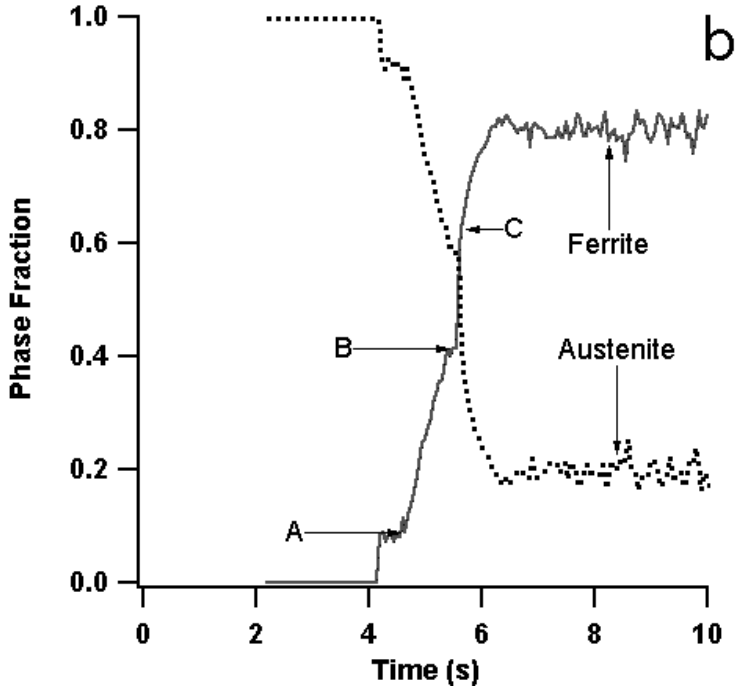
b
Phase Fraction
1.0
0.8
0.6
0.4
0.2
0.0
A
B
C
Ferrite
Austenite
0
2
4
6
8
10
Time (s)

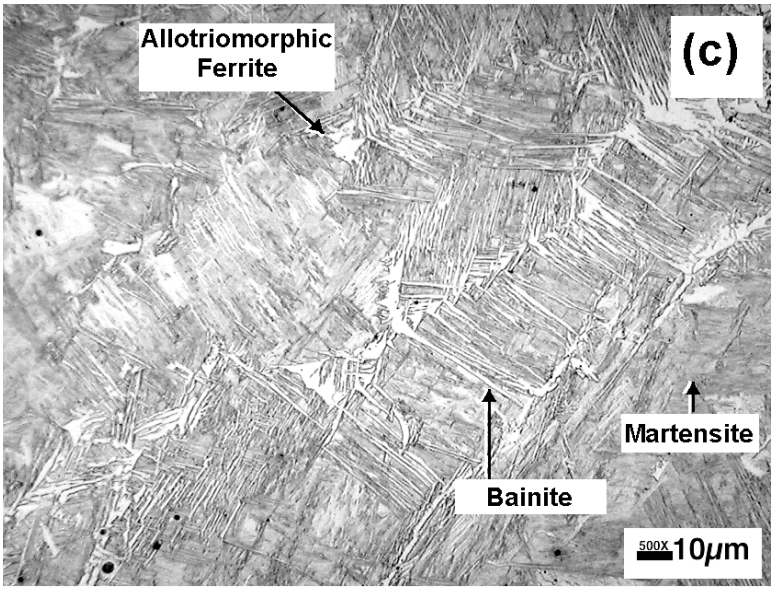


Fig. 6 (*a*) TRXRD data from the rapidly cooled FZ region of Fe-C-Al-Mn spot weld is shown in image format. (*b*) Calculated ferrite and austenite fraction based on integrated area fraction shows the distinct two-stage austenite decomposition. (*c*) Optical micrograph that shows the predominant presence of martensite and small fractions of bainite and allotriomorphic ferrite.

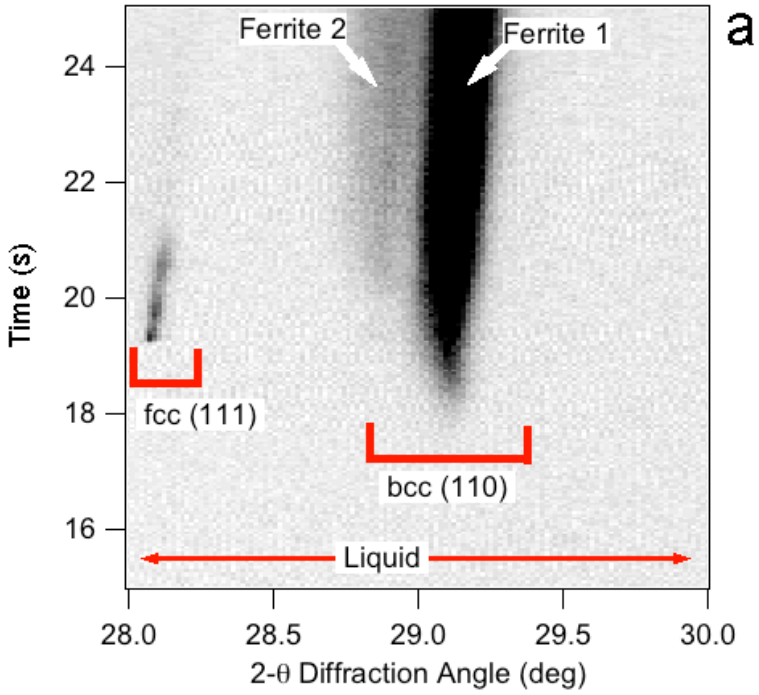
a
Ferrite 2
Ferrite 1
24
22
20
18
16
Time (s)
fcc (111)
bcc (110)
Liquid
28.0
28.5
29.0
29.5
30.0
2-θ Diffraction Angle (deg)

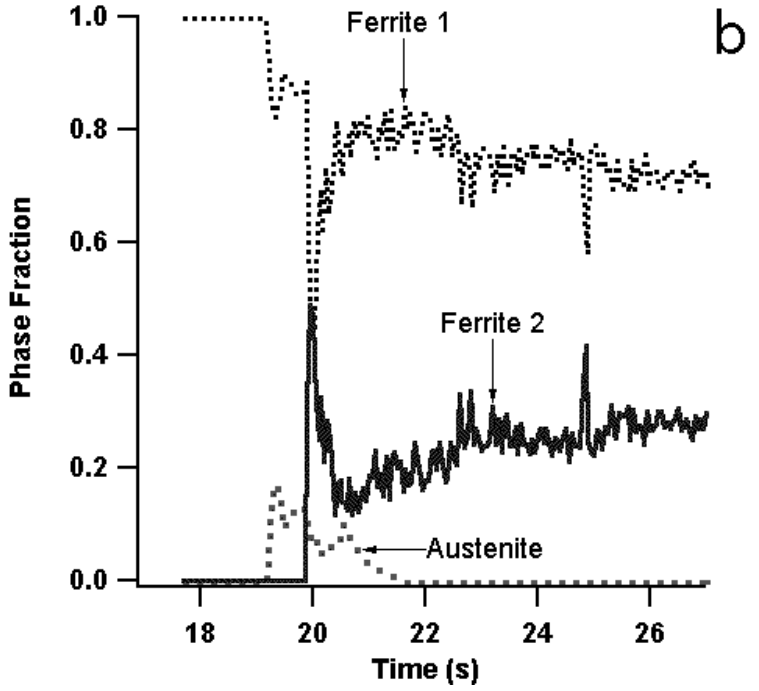
b
Ferrite 1
Ferrite 2
Austenite
1.0
0.8
0.6
0.4
0.2
0.0
Phase Fraction
18
20
22
24
26
Time (s)

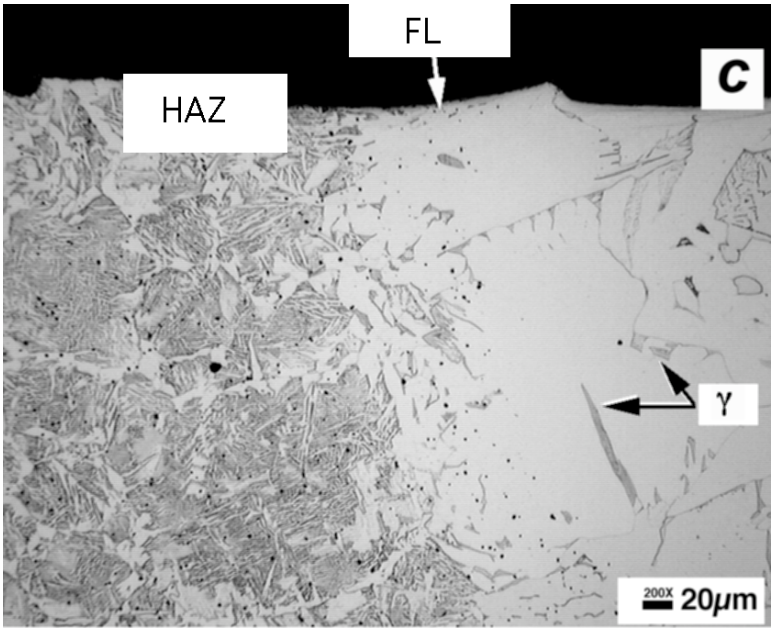


Fig. 7(*a*) TRXRD data from the slowly cooled FZ region of Fe-C-Al-Mn spot weld is shown in image format. (*b*) Calculated ferrite and austenite fractions based on integrated area fraction are also shown. The data shows two types of ferrite, presumably the one that forms from the liquid and another one that forms from decomposition of small austenite that forms in the interdendritic stage. (*c*) Optical micrograph showing the HAZ, Fusion Line (FL) and FZ region of the slowly cooled weld and the presence of coarse δ-ferrite in the FZ can be seen. In addition, the presence of austenite (marked by arrows) in between the ferrite grains can be seen.

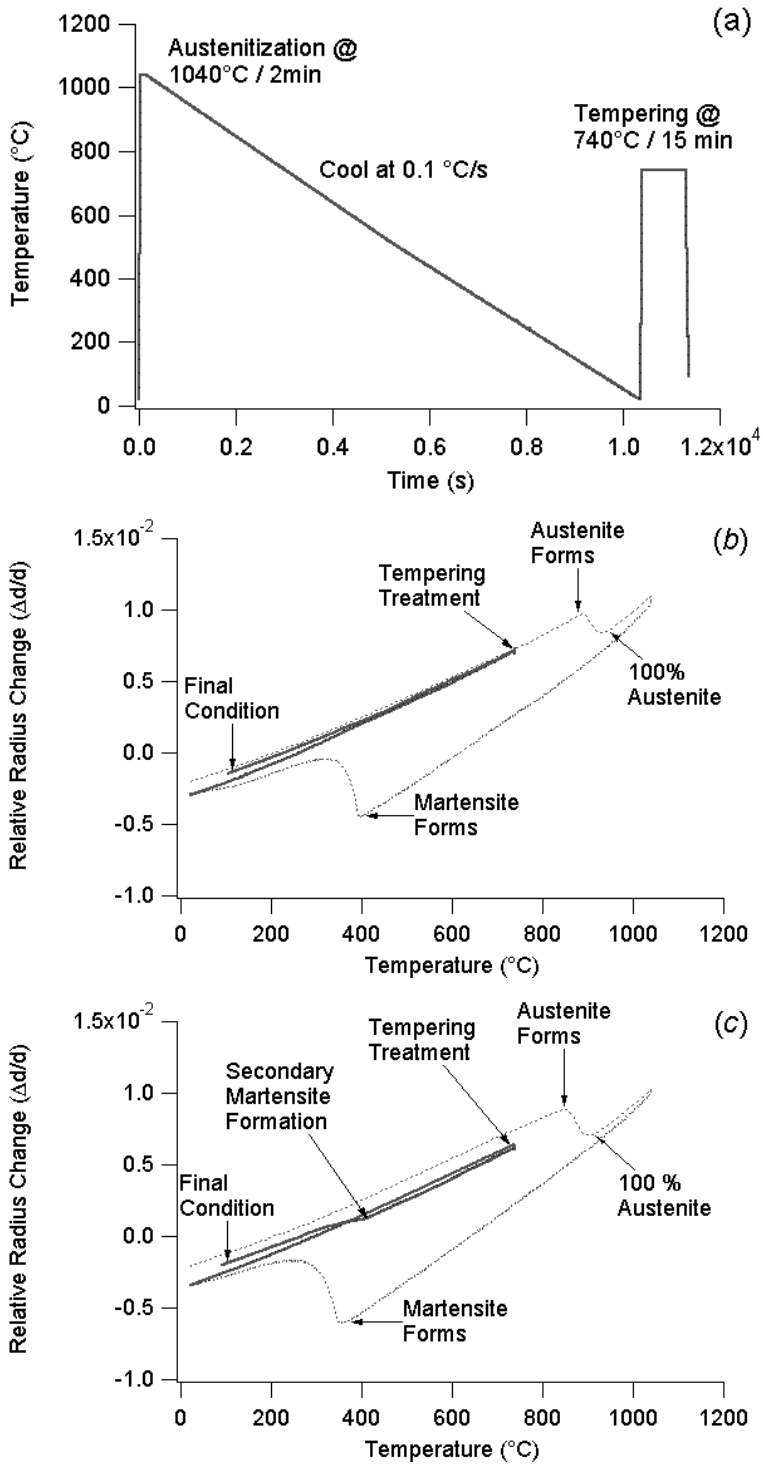


Fig. 8 (*a*) Temperature cycle used for normalizing and tempering used for investigating the microstructural evolution in 9Cr-1Mo-V steels is shown. Dilatometric changes measured, as a function of temperature shows different phase transformation phenomena for (*b*) base metal and (*c*) weld metal sample.

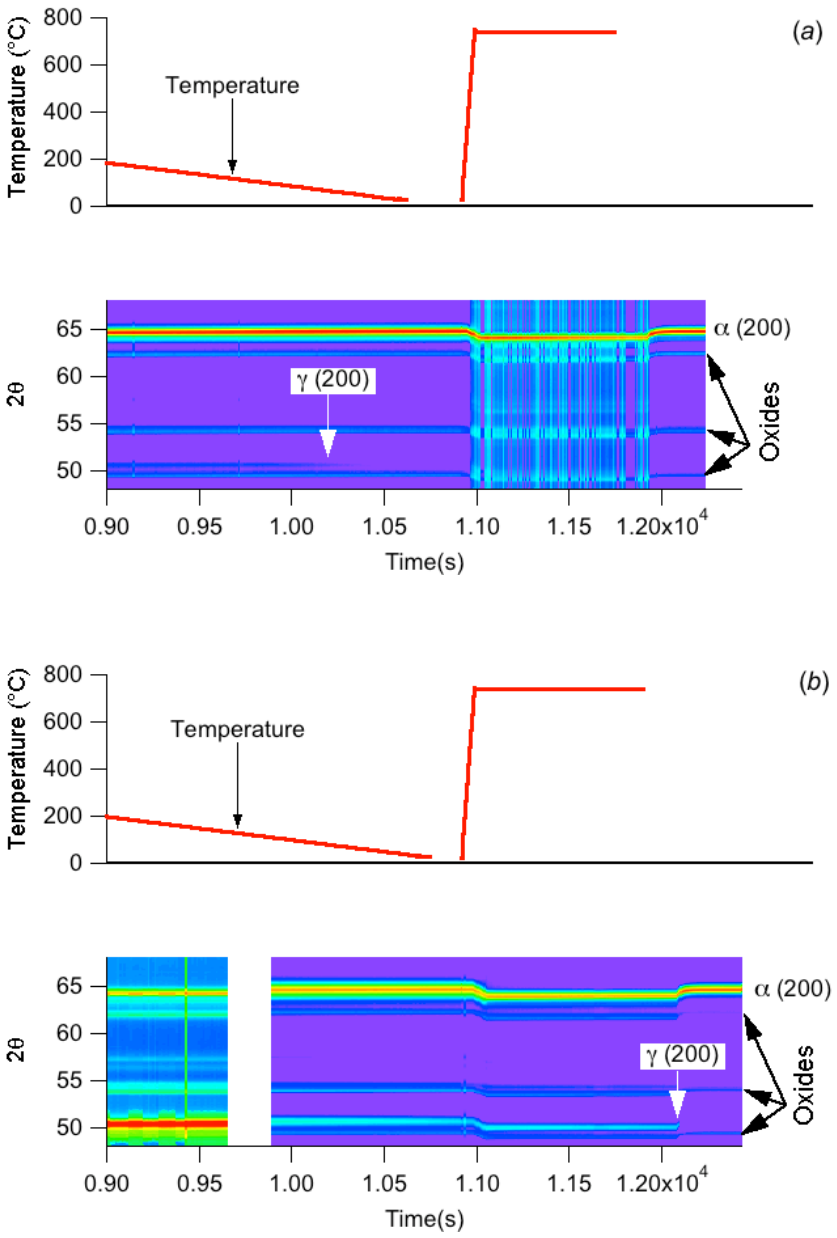


Fig. 9 Variations of temperature and diffraction results from (a) BM and (b) WM regions are shown. Temperature profile shows the later stages of cooling from austenitization treatment and the subsequent tempering treatment. The temperatures during cooling from tempering treatment were not measured, however, diffraction measurements continued. The logarithmic diffraction intensities are presented in image format from both the sample. The 2θ values have been converted to those for Cu K-alpha radiation. Some of the oxide lines are also marked.

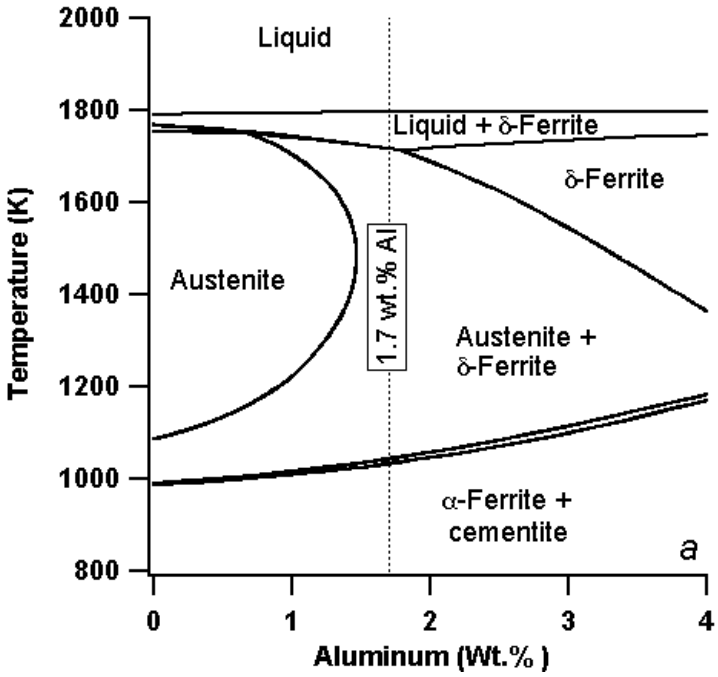
Liquid
Liquid + δ-Ferrite
δ-Ferrite
Austenite
1.7 wt.% Al
Austenite +
δ-Ferrite
α-Ferrite +
cementite
a
Temperature (K)
Aluminum (Wt.% )
2000
1800
1600
1400
1200
1000
800
0
1
2
3
4

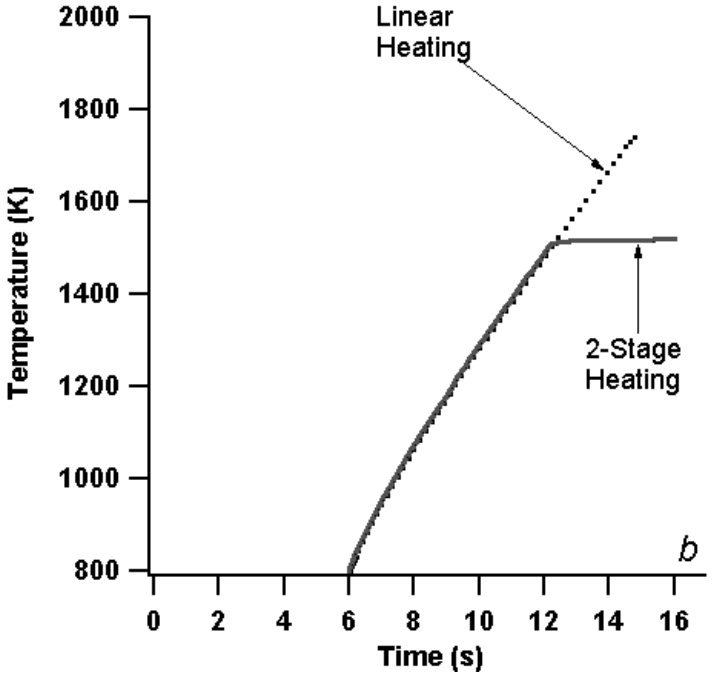
Linear
Heating
2-Stage
Heating
b
Temperature (K)
Time (s)
2000
1800
1600
1400
1200
1000
800
0
2
4
6
8
10
12
14
16

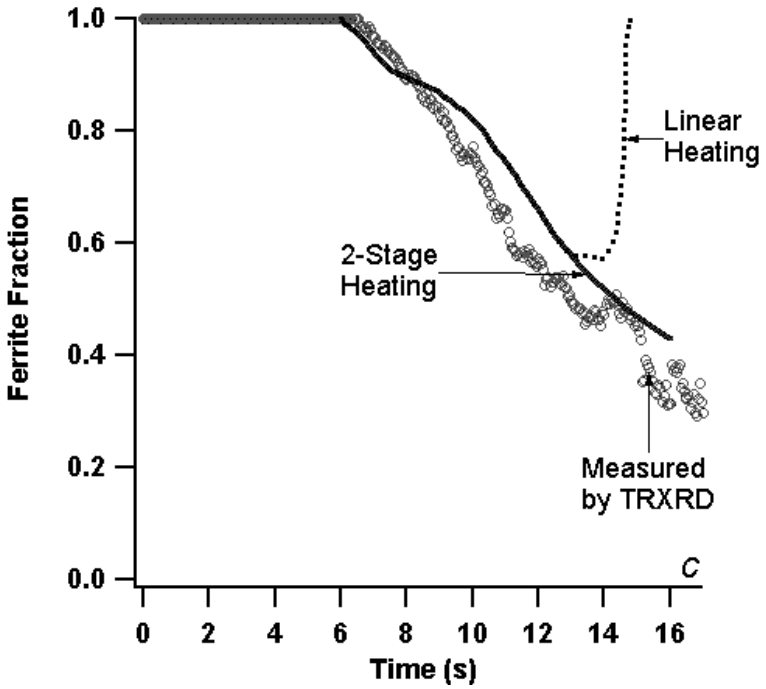


Fig. 10 (*a*) Quasi-binary phase diagram shows the stability of different phases in Fe-C-Al-Mn steel. (*b*) Linear and two-stage heating cycles used for simulating the austenite formation in the HAZ region of the weld are shown. The simulation considered only temperatures above 800°C. (*c*) Comparison of measured ferrite fraction with predicted ferrite fraction for three different heating cycles.

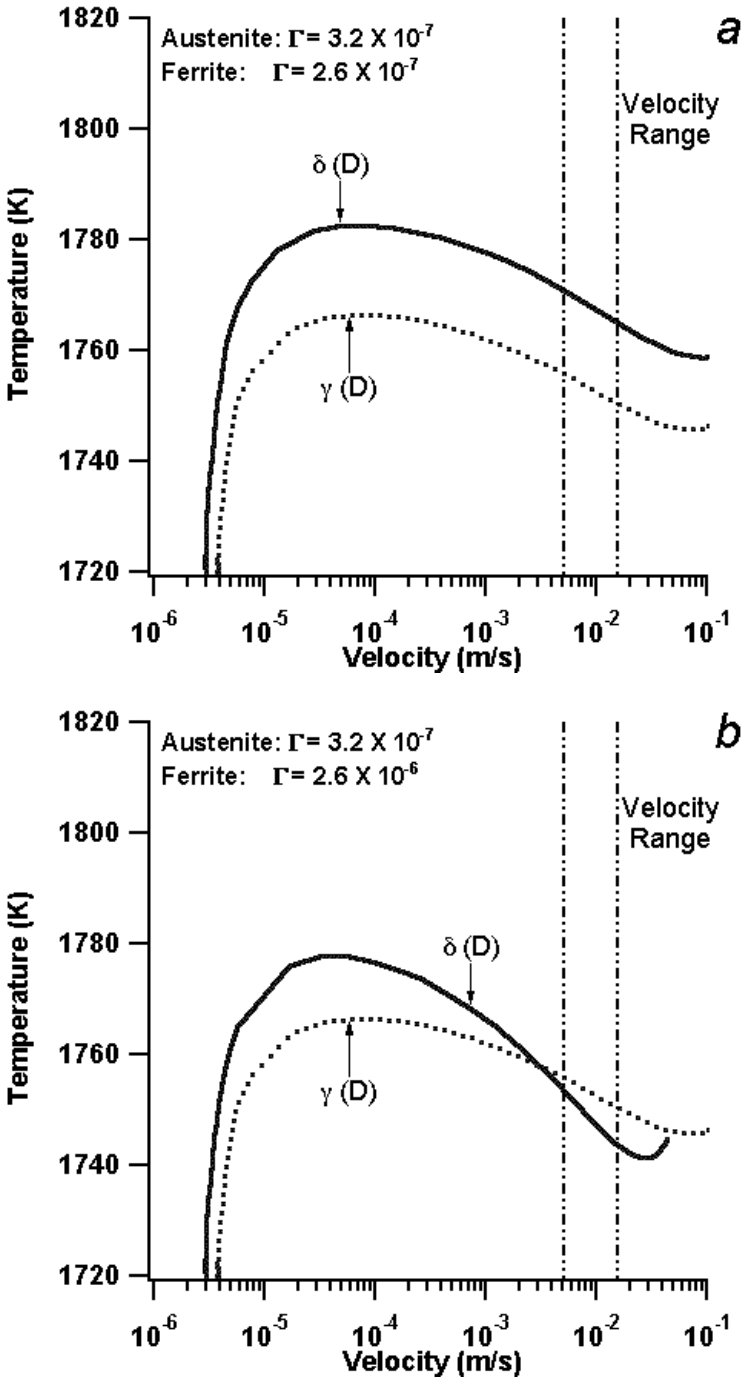


Fig. 11. (*a*) Predicted liquid-δ-ferrite and liquid-γ-austenite interface temperature for dendritic (D) growth as a function of interface velocity (*a*) with standard Γ Gibbs-Thompson coefficient for both phases and (*b*) with modified Γ value for δ-ferrite.

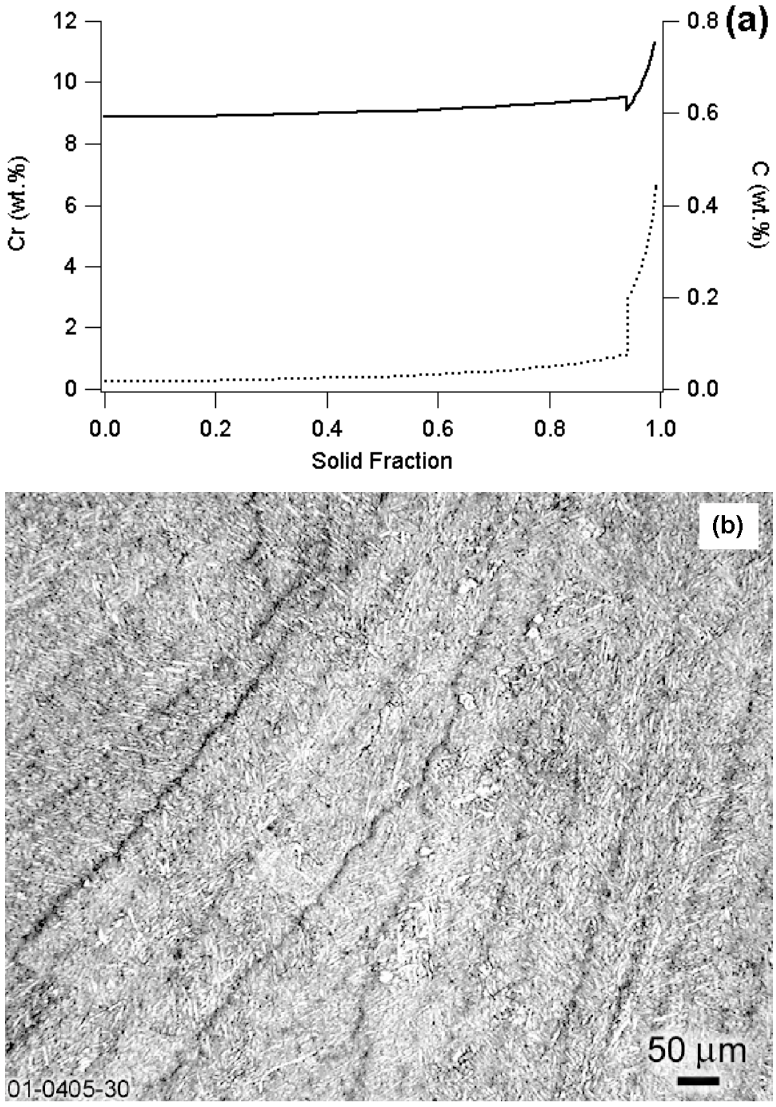


Fig. 12 Predicted variation of Cr and C as a function of solid fraction formed assuming Scheil-Gulliver model and (*b*) optical micrograph of the WM sample with tint etching showing evidence for microsegregation along the prior dendrite boundaries.

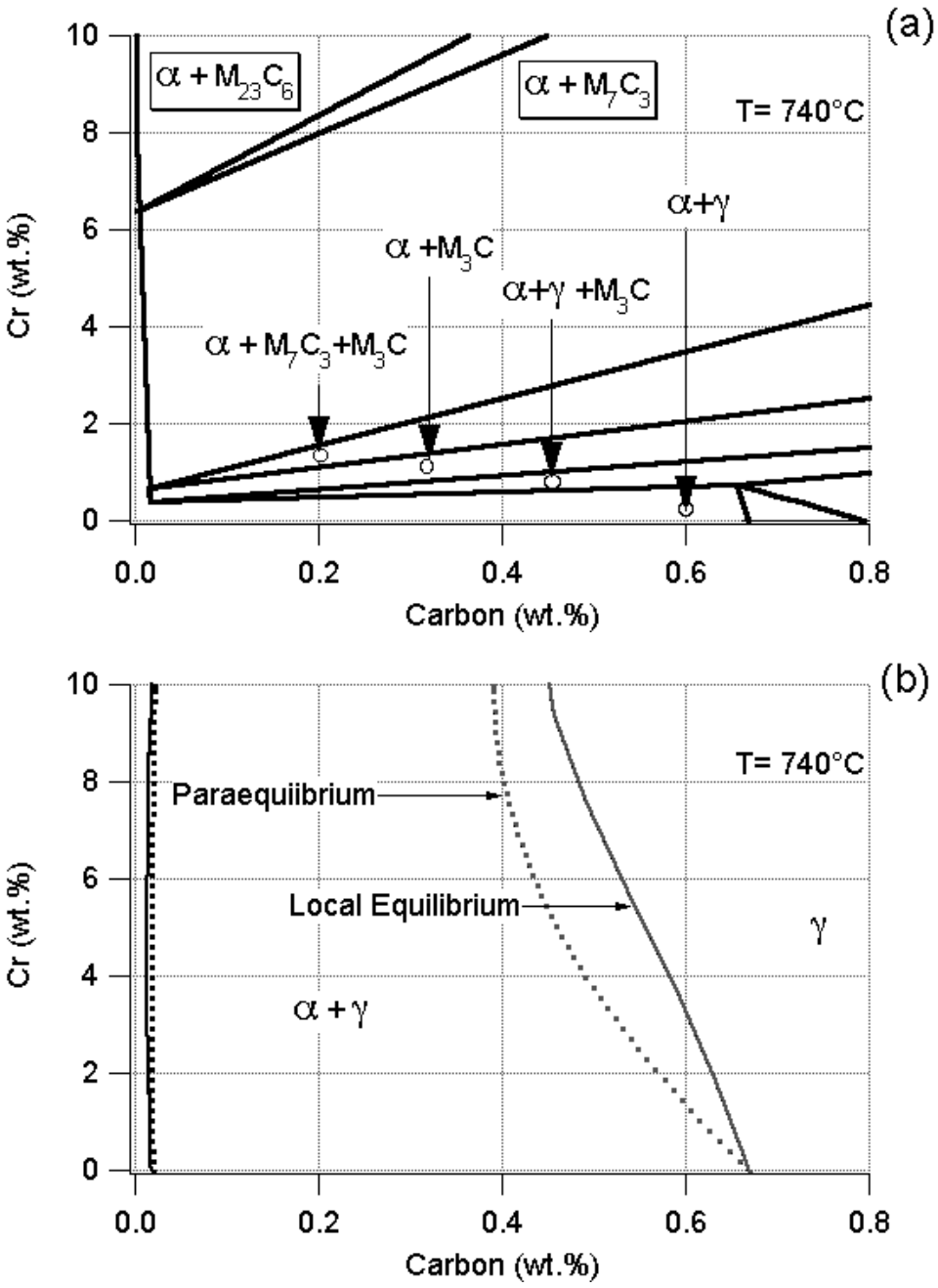


Fig. 13 Calculated local equilibrium phase boundaries considering ferrite, austenite and all carbides are shown. (*b*) Calculated local equilibrium and paraequilibrium phase boundaries considering only ferrite and austenite are shown.

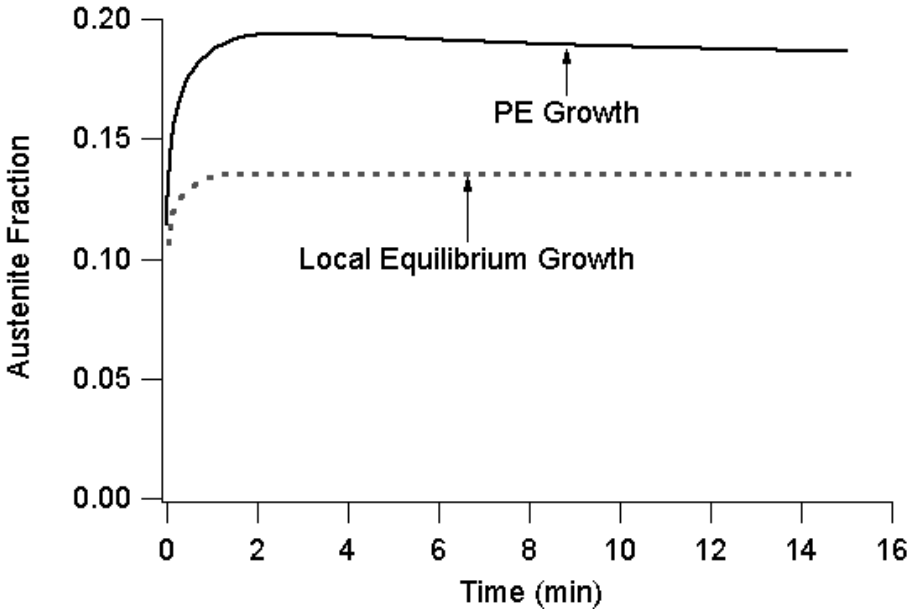


Fig. 14 Predicted increase of austenite fraction at 740°C due to equilibration with martensite that formed during normalizing treatment is shown for both local equilibrium and PE growth condition.